CORA Cork Open Research Archive
Cartlann Taighde Oscailte Chorcaí

Title	Chalcophile element (Cu, Zn, Pb) and Ga distribution patterns in ancient and modern oceanic crust and their sources: Petrogenetic modelling and a global synthesis
Authors	Furnes, Harald;Dilek, Yildirim;Kiseeva, Ekaterina S.
Publication date	2022-05-18
Original Citation	Furnes, H., Dilek, Y. and Kiseeva, E. S. (2022) 'Chalcophile element (Cu, Zn, Pb) and Ga distribution patterns in ancient and modern oceanic crust and their sources: Petrogenetic modelling and a global synthesis', Gondwana Research, 109, pp. 394-415. doi: 10.1016/j.gr.2022.05.008
Type of publication	Article (peer-reviewed)
Link to publisher's version	10.1016/j.gr.2022.05.008
Rights	© 2022, International Association for Gondwana Research. Published by Elsevier B.V. All rights reserved. This manuscript version is made available under the CC BY-NC-ND 4.0 license. - https://creativecommons.org/licenses/by-nc-nd/4.0/
Download date	2026-11-06 19:25:37
Item downloaded from	https://hdl.handle.net/10468/13303

UCC
University College Cork, Ireland
Coláiste na hOllscoile Corcaigh

text file
Click here to access/download;text file;Furnes et al._JGSL Ms_Chalcophile-Final_3152021.docx

Chalcophile Element (Cu, Zn, Pb) and Ga Distribution Patterns in Ancient and Modern Oceanic Crust and Their Sources: A Geochemical Tool to Differentiate Ophiolite Types

Harald Furnes[1], Yildirim Dilek[2] and Ekaterina S. Kiseeva[3]

[1] Department of Earth Science, University of Bergen, Allegt. 41, 5007 Bergen, Norway

[2] Department of Geology & Env. Earth Science, Miami University, Oxford, OH 45056, USA

[3]School of Biological, Earth & Environmental Sciences, University College Cork, Ireland

Corresponding author:

Professor Yildirim Dilek
E-mail: dileky@miamioh.edu

Submitted to:
Journal of the Geological Society of London
Review Paper

30 May 2021

ABSTRACT

We present a global synthesis of Cu, Zn, Pb and Ga contents of mafic rocks from 259 Phanerozoic to Archean ophiolites, which are geochemically classified as subduction-unrelated and subduction-related with various sub-categories. The subduction-unrelated ophiolites include mid-ocean ridge (MOR), and Rift, Continental Margin and Plume type ophiolites, collectively grouped as the R/CM/P sub-category. The subduction-related ophiolites include Backarc (BA), Forearc (FA), Backarc to Forearc (BA-FA), and Volcanic arc (VA) sub-categories. Compositional distribution of these chalcophile elements in different ophiolite sub-categories show that Zn and Ga patterns define subtle changes, whereas Cu and Pb patterns show more pronounced variations. Cu defines a progressive change from the MOR–type through BA, BA-FA, FA and VA types with progressively higher portions of low Cu-concentrations. Pb concentrations display a similar pattern for BA through BA-FA, and FA types, but rather irregular patterns for the R/CM/P and VA types. Thus, mafic subunits in analysed ophiolites define similar trends for Cu and Pb, with a progressive shift towards increasing proportions of low concentration for alkaline basalts, MORB, IAT and boninites. Petrogenetic modelling of the MgO versus Cu, Zn, Pb and Ga distributions in modern oceanic crust and different ophiolite sub-categories show a scatter that can be explained by fractional crystallization of the melts, which were produced by 5-10% partial melting of a variously depleted mantle source. The observed Pb enrichment in the R/CM/P ophiolites was likely caused by crustal contamination. Mantle sources of mafic magmas of the ophiolites were also enriched in Cu and Pb by a combination of subduction-related processes as reflected in the Cu and Pb behaviour patterns of various mafic rock types in the ophiolites.

Key words: Chalcophile elements in ophiolites; ophiolite types and classification; fractional crystallization of basaltic melts; sediment subduction and melting; Cu and Pb enrichment in mafic magmas; slab effects in the melt evolution of SSZ ophiolites.

1. Introduction

Transition metals Cu, Zn, Pb and Ga have been mined extensively in the upper crustal lithologies of many Phanerozoic ophiolites and Precambrian greenstone belts throughout the history (e.g., Galley and Koski, 1999). These elements are widely sought out and used in the industry: Cu is used in many electrical and electronic devices, building construction, wiring, and engines; Zn in galvanizing and as an alloy; Pb mainly in the battery production as well as for many other purposes (e.g., Acharya, 2013), and Ga in the production of smartphones and solar cells (e.g., Sahlström et al. 2017). Gallium as an element does not occur in nature but is usually incorporated in crystal structure of many rock-forming minerals. Although *sensu stricto* lithophile (Goldschmidt, 1937), it is frequently demonstrating chalcophile behaviour and is associated with sulphides, in particular sphalerite (ZnS) (Paradis, 2015; Sahlström et al., 2017). Therefore, further in text we will be referring to Ga as a chalcophile element.

The main sources of these elements are related to metal enrichment and ore mineralization processes in hydrothermal systems along seafloor spreading centers in former ocean basins (e.g., Alt, 1995, Alt et al. 2010; Pirajno et al., 2020) or within island arc – forearc settings of suprasubduction zone tectonic environments (e.g., Hein and Mizell, 2013; Varnavas and Papavasiliou, 2020). Such ore deposits may form at and near the surface of submarine volcanoes, or in the upper stratigraphic and structural levels of submarine magmatic complexes known as volcanogenic massive sulphide deposits (VMS) (Galley et al., 2007). In addition to their economic importance, chalcophile elements, particularly Cu and Pb, are commonly used as geochemical tracers in the melt evolution of mafic magmas in oceanic environments (e.g., Jenner et al., 2015; Wang and Becker, 2015). Stable isotopes of Cu, Ga and Zn are also used widely in studies of planetary geology (Kato and Moynier, 2017; Paniello et al., 2012; Savage et al., 2015; Xia et al., 2019). Therefore, the occurrence and distribution of chalcophile elements in the rock record are scientifically and economically relevant and important for the societies. Some of the best examples of ophiolite – hosted metallic ore deposits of copper, zinc, lead, silver and gold include the Troodos ophiolite in Cyprus (Dilek and Eddy, 1992; Eddy et al., 1998; Hannington et al., 1998; Antivachis, 2015), the Semail ophiolite in Oman (Mahfoud and Beck, 1997), the Khoy ophiolite in Iran (Aftabi et al., 2006), the Mirdita ophiolite in Albania (Dilek et al., 2005; Phillips-Lander and Dilek, 2008; Milushi, 2015), the Løkken (McQueen, 1990) and Karmøy (Grønlie and Logn, 1978) ophiolites in the Norwegian Caledonides, and the Palaeoproterozoic ophiolites in the North Karelia Schist Belt in Finland (Saalmann and Laine, 2014).

One significant question pertaining to the occurrence of chalcophile elements in ophiolites is what parameters and processes control their distribution in ophiolites with different magmatic and tectonic origins. In this study we have examined and analyzed published data on chalcophile element (Cu, Zn, Pb) and Ga distributions in basaltic lithologies and upper mantle peridotites of ophiolites with varying ages, internal structures and tectonic origins. Here, we compare and discuss the distribution of these elements in the investigated ophiolites exposed in different orogenic belts within the framework of our ophiolite classification (Dilek and Furnes, 2011). We have sub-grouped and examined compositionally identified ophiolitic subunits with discrete geochemical affinities (i.e., alkali basalts, mid-ocean-ridge basalts, island arc tholeiites and boninites) in terms of their elemental patterns (in histogram distribution), and then we have modelled partial melting and fractional crystallization trends of their magmas. In order to understand how the distribution of chalcophile elements in ophiolites compare with rock sequences of comparable geochemical affinities in *in-situ* oceanic environments, we have done petrogenetic modeling to decipher the mode of their occurrences in both ancient and modern oceanic lithosphere. We conclude that chalcophile element distribution patterns in mafic lithological units in ophiolites can be used as an additional geochemical proxy to differentiate different ophiolite types in orogenic belts.

2. Ophiolite types and their upper crustal lithologies

An extended characterization and classification of ophiolites, compared to that of the original Penrose classification (Anonymous, 1972), has been presented in Dilek and Furnes (2011). In this recent classification, ophiolites are defined as "*suites of temporally and spatially associated ultramafic to felsic rocks evolved from separate melting episodes and processes of magmatic differentiation in particular oceanic environments*". This definition implies that not all ophiolites have the magmatic kinship between their upper mantle peridotites and crustal units as in a melt – residual relationship, expected from the Penrose definition of an ophiolite; some ophiolites might have formed as a result of multiple partial melting episodes of continually evolved and modified mantle sources in transient tectonic settings (Dilek and Furnes, 2014).

2.a. Phanerozoic ophiolites and their classification

Ophiolites are classified into two main categories based on whether subduction – controlled fluid and melt production contributed to their magmatic evolution: (1) subduction-unrelated, and (2) subduction-related ophiolites. Subduction-unrelated ophiolites include mid-ocean-ridge (MOR), Rift (R), continental margin (CM), and plume (P) types; we categorize the last three in one group as R/CM/P ophiolites. The subduction-related category includes Backarc (BA), Forearc (FA), Backarc to Forearc (BA-FA) and Volcanic Arc (VA) types (e.g., Dilek and Furnes, 2014; Furnes and Dilek, 2017; Furnes et al., 2020), depending on the extent of subducting slab influence in the melt evolution of these ophiolite types. Schematic plate tectonic diagrams showing the major magmatic construction of the oceanic lithosphere, and the architecture and lithology of the various ophiolite types are shown in **Figure 1**. In order to differentiate these different ophiolites in terms of their melt evolution, we have used the elements Ti, V, Y, Zr, Nb, Th, and Yb for geochemical discrimination, either as in various ratio patterns (Nb/Yb – Th/Yb, Nb/Yb – TiO_2/Yb) and element concentrations (Ti – V) (see Pearce, 2014) (**Fig. 2**), or in MORB-normalized element (Nb_N – Th_N) diagrams (see Saccani, 2015). Further information on the geochemical discrimination techniques that we used in this study and more detailed description of the ophiolite types can be found in Furnes et al. (2014. 2015, 2020).

Tectonic extension and thinning during continental rifting results in continental breakup, followed by the formation of an embryonic oceanic crust developing Rift (R) and Continental Margin (CM) oceanic crust. As the rift – drift processes advance, continued extension leads into the onset of seafloor spreading and the formation of a MOR-type oceanic crust. The best examples of MOR – type ophiolites are represented by the Jurassic ophiolites in the Western Alps and in the Northern Apennines (Balestro et al., 2018). A special case of R and CM ophiolites is represented by plume-type (P) ophiolites, whose magmatic construction and melt evolution were affected by proximal plume magmatism during the rift–drift and seafloor spreading stages of oceanic crust development. Some of the best examples of P-type ophiolites occur in the Balkan Peninsula, Anatolia, Iran and in Southern Tibet in the Alpine – Himalayan orogenic belt (Saccani et al., 2015; Yang and Dilek, 2015). These types of subduction-unrelated ophiolites are shown in the lower panel of Figure 1.

Among the subduction – related ophiolite types, the structural architecture of BA ophiolites is similar to that of the mid-ocean ridge generated oceanic lithosphere (Dilek et al., 1997; Eason and Dunn, 2015), although crustal and upper mantle units in these two types may differ geochemically. FA type ophiolites may also share some structural similarities with the MOR oceanic crust but differ from the subduction-unrelated ophiolites because of the presence of intermediate (andesitic) to silicic (dacite and rhyolite) IAT-type extrusive and intrusive rocks, and boninitic (BON) extrusive and intrusive rocks (i.e., Dilek and Thy, 1998, 2009; Dilek and Flower, 2003), which are missing in MOR – ophiolites. The BA-FA oceanic crust forms in continuously extending upper oceanic plates above retreating slabs, and constitutes a hybrid type between the BA and FA generated oceanic crust (i.e., Mariana Trough through Mariana Forearc; Kato et al., 2003). The volcanic arc oceanic crust develops as a result of a prolonged period of magmatic construction, 20 to 30 million-years in comparison to other SSZ types of oceanic crust formation in ~10 million years, above subducting oceanic slabs (Dilek and Furnes, 2011; 2014). The middle to lower crust of a volcanic arc oceanic crust is dominated by abundant diorite, tonalite and granodiorite intrusions (see **Fig. 1** of Furnes and Dilek, 2017), and the upper crust by thick accumulations of basaltic, dacitic and rhyolitic submarine to subaerial volcanic and volcaniclastic rocks (see **Fig. 1** of Furnes and Dilek, 2017). The thickness of a volcanic arc ophiolite may, therefore, be considerably larger than the other subduction-related ophiolite types, as in the Jurassic Smartville arc ophiolite (~ 20 to 25 km in thickness) in the Northern Sierra Nevada Foothills in California (Dilek, 1989a, 1989b; Godfrey and Dilek, 2000). A simplified version of the various subduction-related ophiolite types is presented in the upper panel of **Figure 1**.

2.b. Archean ophiolites

One of the presently contentious issues in the Precambrian geology is when plate tectonics was initiated (see Dewey et al. 2021, for a recent overview). Since ophiolites are among the first-order indicators in support of the operation of plate tectonics in earth's history, a corollary to the question above is whether there are Archean ophiolites preserved in the rock record. Several age thresholds have been proposed for the onset of plate tectonics over the last several decades. These time windows range from 0.8 Ga (Hamilton,

2011) to 4.2 Ga (Hopkins et al., 2008), with several other models proposing the time span of 2.9 to 3.2 Ga for the onset of Phanerozoic – type rigid plate tectonics (Palin et al., 2020; Dhuime et al., 2015; Condie, 2018; Brenner et al., 2020; Palin and Santosh, 2021). In a recent review of Eoarchean supracrustal belts, Windley et al. (2021) have distinguished between two types of plate tectonics: Accretionary Cycle Plate Tectonics and Wilson Cycle Plate Tectonics. They have suggested that the former has been operating since 4 Ga, whereas the latter became predominant in earth history around 2.7-2.5 Ga. The discussion of the mode of the Archean tectonics is beyond the scope of this paper. However, the results of our own field–based structural, geochemical and petrological studies in the Barberton greenstone belt (ca. 3.1-3.6 Ga; see De Wit et al., 2011) and the Isua greenstone belt in SW Greenland (ca. 3.7-3.8 Ga; see Nutman et al., 1997; Furnes et al., 2007, 2009) indicate that oceanic crust formation, albeit in different modes and tempos from those in the Phanerozoic Eon, must have occurred in the Archaean rock record (Furnes et al., 2015; Polat et al.,2007; Ordonez-Calderon et al., 2009). Rates of horizontal and vertical tectonic processes derived from the Barberton greenstone belt are similar, well within an order of magnitude, to those encountered across modern oceanic and orogenic terrains (de Wit et al., 2018). Therefore, all the pre–3 Ga mafic–ultramafic sequences included in this study are considered as ophiolitic in origin (see **Supplementary Table 1**). Relevant discussions on the Archaean ophiolite types are presented in Dilek and Polat (2008) and Dilek and Furnes (2011).

3. Ophiolite types and mineralization

Ophiolites represent an important source for Cu, and to some extent for Zn and Pb, as well as Ag and Au in the recorded human history (Dilek and Furnes, 2014), and these elements are in general spatially and temporally associated with volcanogenic massif sulphide deposits (VMS) See Supplementary Table 1 for these associations. An important question that is relevant to the topic of this paper is whether any of the ophiolite types, discussed briefly above has a preference for VMS deposit formation and associated mineralization processes.

VMS deposits are common in both ophiolites and modern oceanic crust. They are known to have developed in hydrothermal systems (e.g., Oudin and Constantinou, 1984; Hannington et

al., 1998) along active seafloor spreading centers of the mid-ocean ridges (e.g., Shanks III, 2012; German et al., 2016) and backarc basins (e.g., Anderson et al., 2017). Oceanic hydrothermal systems involve convective circulation of seawater through the modern oceanic crust above an active magma chamber and contain recharge, reaction, and discharge zones (e.g., Alt, 1995). In a recharge zone, seawater penetrates through the faulted and fractured, young oceanic crust and progressively causes alteration and element mobility on its tectonically – induced descent to the high-temperature reaction zone in the lower crust above the magma chamber. Then, during the up-flow of super-heated fluids in a discharge zone within the oceanic crust, epidosites and quartz-sulphides become precipitated as VMS deposits.

VMS deposits have been classified into five categories according to the origin and nature of their host-rocks: (1) mafic; (2) bimodal-mafic; (3) mafic-siliciclastic; (4) bimodal-felsic; and (5) bimodal-siliciclastic (Barrie and Hannington, 1999). This is a chemical classification of the most primitive (mafic) to the most evolved (felsic) host-rock associations in VMS deposits. The depth of a melt lens, which drives the hydrothermal circulation responsible for the formation of mafic VMS deposits, is approximately 2 to 3 km below the spreading axis (e.g., Ridley, 2012). Nearly 80 % of the 259 ophiolites examined in this study (**Supplementary Table 1**) are Phanerozoic, 11% Proterozoic, and 9% Archean in age. Approximately 24% of all these ophiolites (64 examples) belong to the subduction-unrelated and 76% (195 examples) to the subduction-related group. Most of these ophiolites and the majority of Phanerozoic ophiolites in different orogenic belts belong to the mafic–type VMS deposits (Barrie and Hannington, 1999) in terms of their mineralization features. Mafic–type VMS deposits contain more than 75% mafic and less than 1% felsic rocks. Some of the Archean ophiolites and greenstone belts belong to the VMS bimodal-mafic–type (Barrie and Hannington, 1999), which is defined as having >50% mafic rocks and >3% felsic volcanic rocks with a mafic/felsic volcanic rock ratio of 3 to 1. The VMS mafic–type is rich in Cu, whereas the VMS bimodal-mafic–type is rich in Zn and Pb (Barrie and Hannington, 1999).

Spreading rate and seafloor morphology of the oceanic ridges vary in response to the spatial and temporal interactions between tectonic processes and magma supply rates (Dilek et al., 1998) that in turn control the dynamics of hydrothermal convection and sulphide deposition (Hannington et al., 1995; Schulz, 2012). At fast-spreading mid-ocean ridges, such as the East Pacific Rise, sulphide deposits may be abundant but small in size, whereas at slow-spreading

centers there may be a few but much larger sulphide deposits, such as the Trans-Atlantic Geotraverse (TAG) hydrothermal field on the Mid-Atlantic Ridge at the 26°N Latitude in the Central Atlantic Ocean (e.g., Hannington et al., 1995, 2011; Schulz, 2012).

Backarc seafloor spreading systems share similar structural features as in slow- and fast-spreading mid-ocean ridges, but they may additionally have several other operative processes related to subduction (e.g., Anderson et al., 2017; Evans et al., 2017). The oceanic crust along backarc spreading centers may be segmented, as seen in the East Scotia (Fretzdorff et al., 2002) and the Mariana (Anderson et al., 2017) backarc basins. In the latter example, hydrothermal venting occurs in every segment, the character of which may vary from tectonically dominated to magmatically-dominated, reminiscent of slow- and fast-spreading mid-ocean ridge systems, respectively (Dilek et al., 1998). In the case of magmatically-dominated spreading segments with shallow-level axial magma chambers, the entire oceanic crust behaves in a ductile fashion and the hydrothermal circulation is restricted to this shallow crust (Devey et al., 2010). For tectonically dominated spreading segments, on the other hand, the more brittle character of the oceanic crust and deeper and long-term hydrothermal circulation patterns commonly result in the formation of large VMS deposits (Pertsev et al., 2012). Regarding the concentration of Cu, Zn, and Pb (and several other chalcophile elements) in hydrothermal fluids, large variations may develop as a result of major changes in fluid fluxes in the entire subduction zone environment as measured at several sites in the Lau Basin (Evans et al., 2017).

It appears that the physical conditions, including tectonic and magmatic processes, for sulphide mineralization in VMS deposits, are much the same in major oceans as well as in backarc basins. However, additional element supply from subducting slabs may possibly account for backarc ophiolites to be more favourable for the formation of large VMS deposits. Galley and Kosky (1999) investigated more than 200 ophiolites worldwide and found that about 10% of these examples contain significant VMS mineralization. The most sulphide-rich VMS examples of those listed in Galley and Kosky (1999) are subduction-related ophiolites. Thus, to place a few of the richest ones in the present geochemical classification scheme of ophiolites (see Fig. 1, and Furnes et al. 2014; 2020), the following may be listed: Troodos, Cyprus (BA-FA); Oman (BA-FA); Løkken, Norway (BA); Kure, Turkey (BA); Betts Cove (FA) and Lush Bight (FA), Newfoundland, Canada.

4. Elemental patterns of different ophiolite types

We used in our compilation the geochemical data from 259 ophiolites, occurring in different orogenic belts and having a wide range of igneous ages. Geochemical characteristics of these ophiolites provide important insights into their mantle melt sources within different time windows in earth history (Dilek and Furnes, 2014). The examples include the Triassic, Jurassic and Cretaceous ophiolites in the Alpine-Himalayan orogenic Belt (n=117), the Late Proterozoic to Triassic ophiolites in the Central Asian Orogenic Belt (n=45), the Mesozoic ophiolites in the Western Pacific and North American Cordillera belts (n=12), the Paleozoic ophiolites in the Qingling-Qilian-Kunlun Belt in northern China (n=7); the Cretaceous to Neogene Indonesian Belt (n=5), the Andes (n=4), the Silurian Uralides (n=2), the Ordovician to Devonian Central European Variscides (n=1), the Cambrian to Devonian Caledonides and the Appalachians (n=12), the Cambrian to Devonian to Tasmanides (n=2), and ophiolites within Proterozoic (n=31) and Archean (n=21) greenstone belts.

All these ophiolites have been classified as either subduction-unrelated or subduction-related complexes. We have subdivided them into different types on the basis of the above-mentioned classification; details of this classification are further described and illustrated in the following publications: Furnes et al. (2014, 2015, 2020), and Furnes and Safonova (2019). We have also summarized the relevant information related to their mantle and crustal lithologies, the orogenic belts in which they occur, and the appropriate references in **Supplementary Table 1.**

For characterization of elemental patterns as presented below (**Figures 3 through 8**), we use histograms. Given the appropriate scaling (bins), histograms provide the visually best information that is needed to characterize and compare the distribution of elements. For all the histograms the frequency is expressed as percentages, instead of the absolute number of samples, thus making datasets of different sizes comparable. The applied nomenclature of the different patterns is as the following: (1) bell-shaped (also referred to as symmetric or unimodal); (2) right-skewed (increasing frequency of data towards lowering values); (3) irregular (no particular patterns, or symmetric); (4) bimodal (two peaks).

4.a. Cu patterns

305

306 **Figure 3** shows histograms of the subduction-unrelated (**Fig. 3A and B**) and
307 subduction-related (**Fig. 3A C and F**) ophiolites, based on a compilation of 4005 Cu analyses.
308 The MOR–type ophiolite histogram defines nearly a bell–shaped pattern, with an average Cu-
309 value of 62 ppm. The R/CM/P–type ophiolites histogram shows a similar pattern, but slightly
310 skewed to the right with a less distinct mode. The average Cu-value of 80 ppm in these
311 ophiolites is also significantly higher than that of the MOR–type ophiolites.

312 The Cu-histogram patterns of the subduction-related ophiolite types differ from the
313 subduction-unrelated in that they all have their highest concentration in the lowest Cu-
314 intervals and are all right skewed. This pattern shows a gradual increase in Cu contents from
315 the BA type through the BA-FA and FA types and is most distinctive in the VA type
316 ophiolites (**Fig. 3 C-F**).

317

318 ***4.b. Zn patterns***

319

320 The Zn-histogram patterns, based on 4470 analyses, are characterized by a typical bell-
321 shaped pattern (**Fig. 4**), and the subduction-unrelated and subduction-related ophiolite types
322 show only minor differences. The FA type histogram defines a slightly higher proportion of
323 the two lowest Zn intervals, whereas the VA type shows a relatively high proportion of the
324 highest Zn interval (> 200 ppm), and thus also the highest average value (127 ppm).

325 ***4.c. Pb patterns***

326

327 The Pb-histograms, based on 2978 analyses, define profoundly different patterns for the
328 different ophiolite types of the two main categories (**Fig. 5**). For the two subduction–unrelated
329 ophiolite types (A, B) the MOR type histogram is highly right skewed and nearly half of the
330 data plot in the lowest Pb-interval. The R/CM/P type histogram shows a uniform pattern with
331 two slightly higher peaks in the middle and at the right end (highest value) of the histogram.
332 The latter also has a considerably higher average Pb value (7.3 ppm) than that of the MOR type
333 (2.4 ppm). The Pb-histograms of the subduction-related ophiolites define progressive right
334 skewed patterns of the BA, to the BA-FA and FA subtypes (**Fig. 5 C–E**). The Pb-histogram of

the VA type shows a uniform pattern similar to that of the R/CM/P type, and with the highest Pb population at the right end (highest value) (**Fig. 5 F**). It also has by far the highest average value of 7.1 ppm.

4.d. Ga patterns

The Ga histogram is based on 2269 analyses and defines a bell-shaped pattern. There is little difference between the subduction-unrelated and subduction-related ophiolite types on this histogram (**Fig. 6**). The average Ga-values range between 14.7 to 17.2 ppm.

5. Elemental patterns of the different rock types of ophiolites

Mafic lithological units in most ophiolites are compositionally made of alkaline basalt to MORB, IAT and boninite affinities (Dilek et al., 2008; Dilek and Thy, 2009; Dilek and Furnes, 2011; 2014; Furnes et al., 2014, 2015, 2020; Saccani et al., 2018; Furnes and Safonova, 2019). This is particularly the case for suprasubduction zone ophiolites (Yu et al., 2020). In the subduction-unrelated ophiolites the common basalt types include tholeiitic basalt for the MOR type and alkaline basalt for the R/CM/P type ophiolites. For the subduction-related ophiolites, on the other hand, the crustal lithologies generally consist of two or more of the four compositional groups, ranging from alkaline basalt to tholeiitic basalt (MORB), island arc tholeiite (IAT), and boninite. The proportion of each of these mafic components within an ophiolite determines the ophiolite type as described earlier. For the ophiolites examined in this study, each of these rock compositions has been selected following the methods of Pearce (2014) and Saccani (2015), as applied in Furnes *et al*. 2014, 2015, 2020. The Cu, Zn, Pb and Ga histograms for each type (alkaline basalt, MORB, IAT and boninite) are presented in **Figure 7**.

Alkaline basalts: The Cu histogram defines a combination of bell-shaped to slightly right skewed patterns, whereas the Zn and Ga histograms show typically bell-shaped patterns. The Pb histogram appears irregular and bimodal, with a moderately high proportion of the highest bin (> 12 ppm Pb).

MORB: The Cu histogram is right skewed, with four lowest bins defining a uniform pattern. The Zn and Ga histograms are bell-shaped, whereas the Pb histogram is right skewed.

366 **IAT**: The Cu histogram shows mainly a bimodal pattern as defined by the four lowest
367 bins, and otherwise a right skewed pattern. The patterns of the Zn and Ga histograms are bell
368 shaped, whereas the Pb histogram displays typically right skewed patterns.
369 **Boninite**: The Cu, Pb and Ga histograms are all right skewed, and are most profoundly
370 defined by the Pb pattern. The Zn histogram is bell shaped, as well as slightly right skewed.
371
372 ## 5. Elemental patterns of upper mantle sources
373
374 The upper mantle geochemical data on the distribution of Cu, Zn, Pb and Ga are based
375 on the ophiolites occurring predominantly in the Alpine-Himalayan orogenic belt, with
376 additional data from several other orogenic belts and Precambrian greenstone sequences. In
377 addition, some data from mantle xenoliths hosted in basalts exposed on some oceanic islands
378 and in modern oceanic crust have also been included in our database. In the literature, host
379 mantle rocks are described as unspecified peridotite, lherzolite, harzburgite, dunite, and
380 serpentinite; hence, we use the same terms here. The references to the upper mantle lithologies
381 and the related published information are provided in Supplementary **Table 2.**
382 **Figure 8** shows histograms of the collected data on the above-mentioned elements in
383 upper mantle lithologies. For Cu most of the data are described as harzburgite and lherzolite,
384 and the histograms define a right skewed pattern. The highest population is in the 0 to 5 ppm
385 range and is dominated by harzburgite; the majority of the peridotite and dunite host rocks are
386 also concentrated in this Cu-range. Lherzolite, on the other hand, defines the highest
387 population in the 21-25 Cu-interval, which is in a good agreement with the estimates proposed
388 for the Earth's mantle (20-30 ppm) (McDonough and Sun, 1995; Palme and O'Neill, 2013). A
389 gradual decrease in the Cu-population is shown as the Cu content increases.
390 The patterns of the Zn histogram define bell-shaped distribution, and the peak defined
391 by the 41-50 ppm-interval has the highest population of peridotite, harzburgite and lherzolite.
392 The histogram of the Ga populations with the various concentration intervals defines an
393 irregular distribution. The highest Ga-contents of harzburgite and dunite occur in the 0 to 2
394 ppm range, but in a marginally higher range (1-3 ppm) for lherzolite. Peridotite makes a
395 significant proportion and defines a normal population with a peak in the 1.5 – 2.0 ppm
396 interval. The compiled mantle source concentrations of Zn and Ga in this study are lower in

comparison to the proposed upper mantle value of 53.5 – 55 ppm for Zn and a substantially lower than the average mantle value for Ga (4 – 4.4 ppm) (McDonough and Sun, 1995; Palme and O'Neill, 2013).

The Pb-histogram defines a typical right skewed pattern, similar to that of Cu, with the highest population in the < 0.1 ppm-interval, defined predominantly by unspecified peridotite and harzburgite. The estimated upper mantle value for Pb is 0.150 to 0.185 ppm, more than 1.5 times higher than the highest population; however, it is not possible to exclude potentially high uncertainties in the Pb analysis of bulk – rock peridotites. Additionally, it should be noted that a relatively high proportion of harzburgite shows Pb-contents higher than 1 ppm (in the range of 1 to 5.6 ppm). As a general observation, harzburgite, peridotite, serpentinite and dunite define lower element-intervals for all elements than do the lherzolite, particularly for Cu and Pb. But, depleted mantle, represented by harzburgite, is the most common source material for ophiolites.

6. Alteration and element mobility

Most of the ophiolites examined in this study underwent seafloor alteration and lower greenschist facies metamorphism prior to their emplacement into continental margins (Furnes & Safonova, 2019; Furnes et al. 2020). During seafloor alteration and low-grade metamorphism of basaltic rocks in ophiolites, most major oxides (e.g., FeO, MgO, CaO, Na_2O and K_2O) and several trace elements (e.g., Cs, Ba, Rb, Sr) experience some sort of mobility, either as loss or gain (e.g., Furnes et al., 2012, and references therein). Of the elements considered here, Cu generally becomes mobilized (Gillis and Thompson, 1993) and progressively depleted with increasing epidotization (Wyborn, 1987; Gregory, 2006), for epidote can only accommodate up to 10 ppm Cu (Craw et al., 1997). Thus, during the epidotization process Cu may migrate and get enriched elsewhere within the oceanic crust sequence. Zinc may also become mobilized to some extent and get depleted in the source during alteration and metamorphism, but to a lesser extent than Cu (Gillis and Thompson, 1993; Jowitt et al., 2012). Other investigations have suggested, on the other hand, that Zn does not show any mobilization during the alteration of basalt (Hart et al., 1974), or that it may rather get enriched during low – temperature alteration (Fowler and Zierenberg, 2016). Lead

may exhibit both loss or gain during alteration and low-grade metamorphism, and like Zn, it may get enriched at low-temperature alteration (Fowler and Zierenberg, 2016). Examination of hydrothermal fluids from the Juan de Fuca ridge and the Trans-Atlantic Geotraverse (TAG) hydrothermal field on the Mid-Atlantic ridge shows a strong correlation between Ga and Zn (Metz and Trefry, 2000), indicating that they behave similarly during alteration.

7. Discussion

Figures 3 through **6** demonstrate the histogram patterns of different ophiolite types in the subduction-unrelated and subduction-related categories, with respect to the elemental behaviour of Cu, Zn, Pb and Ga. This compilation shows that Cu and Pb patterns differ significantly among different ophiolite types, whereas Zn and Ga patterns hardly display any differences. However, even though these histograms are well suited for demonstrating differences in elemental distribution among different ophiolite types, they do not provide any insights for a petrogenetic evaluation of ophiolitic magmas with regard to element distributions. Hence, we have plotted Cu, Zn, Pb and Ga values against MgO contents for petrogenetic modeling. The results are shown in **Figures 9** through **12**.

8.1. Petrogenetic behavior of Cu, Zn, Pb and Ga

We compiled literature data on fresh mafic rocks (volcanic glass and crystalline whole – rock samples), which were collected from modern oceanic environments, in order to compare with the data from basaltic rocks in the examined ophiolites. The rock types considered for this modelling include alkaline basalts, mid-ocean ridge basalts (MORB), backarc island arc tholeiitic (IAT) basalts, and boninites (see **Supplementary Table 3**). Most of the geochemical data, particularly the MORB data, are from fresh volcanic glass samples, and thus the patterns of the four elements (Cu, Zn, Pb, and Ga) versus MgO contents are considered to be primary in nature. However, some of the crystalline whole–rock samples have higher MgO than the glassy samples and may thus represent cumulate mafic lithologies. Hence, the fields enveloped by the blue line, representing the distribution of different magmatic types may not be precise. We have stated above that Mg is mobile during alteration and metamorphism. During chloritization at high temperature hydrothermal

459 alteration, the MgO content of basalts becomes enriched. However, Nakamura et al. (2007)
460 have shown that the MgO-enrichment is entirely negligible compared to the MgO-range, as
461 shown in **Figures 9 through 13**.

462

463 *8.1.1. Distribution in Bowen diagrams*

464

465 The Cu distribution of basaltic rocks of the modern oceanic crust defines a broad band
466 with decreasing values as MgO contents decrease, owing to sulphide precipitation and very
467 high compatibility of Cu in sulphides (e.g., Kiseeva and Wood, 2013, 2015). Boninites show a
468 weak opposite trend, indicating no sulphur saturation in their melts (**Fig. 9A**). Most of the IAT
469 basalts plot in the same area as the MORBs but some of the IAT data extend to low MgO
470 values (< 5wt.%), defining a trend. The Cu-distribution of the ophiolite data is shown in **Fig.**
471 **9B**. Most of the data (88%) plot within the field defined by the modern oceanic crustal rocks,
472 but a high proportion of the boninitic as well as some of the IAT data define lower values.

473 The Zn distribution in the basaltic modern oceanic crustal rocks exhibits a well-defined
474 negative trend against the MgO values. This can be explained by the incompatible character of
475 Zn that has partition coefficients (D's) for plagioclase/melt and clinopyroxene/melt below 1
476 (Bédard, 2006; Davis et al., 2013). Boninites appear to have an opposite trend that may be
477 related to the crystallization of olivine, in which Zn is compatible (Foley et al., 2013; Le Roux
478 et al., 2015) (**Fig. 10A**). This is opposite to the Cu pattern. At any MgO content, a substantial
479 part of the Zn data for the IAT rocks shows lower values than those of the MORBs. The
480 ophiolite data plot predominantly (91%) within the field defined by the modern oceanic crustal
481 rocks, and only few of the boninitic samples plot above the Zn envelope (**Fig. 10**).

482 The Pb distribution in the basaltic rocks of the modern oceanic crust defines a broad
483 band, with rapidly increasing values as the MgO contents decrease (**Fig. 11A**). This pattern is
484 consistent with the highly incompatible character of Pb, which has very low partition
485 coefficients (D's) into silicates (≤ 0.5) and relatively low D's into sulphides (~7 – 26) for the
486 P-T conditions (Kiseeva and Wood, 2015). The boninites, on the other hand, show little
487 variation with decreasing MgO contents. For the ophiolites, 88% of the data plot within the
488 field defined by the modern oceanic crustal rocks, and it is mainly the boninitic and IAT rocks

that plot outside the field (**Fig. 11B**). The Ga distribution in the basaltic and boninitic rocks shows a negative trend against the MgO values (**Fig. 12A**), with 81% of the ophiolitic rocks plotting within the field of the modern oceanic crustal rocks (**Fig. 12B**). The 19% that plot outside the Ga envelope are, however, rather close to the envelope defining the field of modern oceanic crustal rocks. The behaviour of Ga in basaltic systems is relatively similar to that of Zn, with a big difference in its lower compatibility in olivine but higher compatibility in plagioclase (see **Table 1**). Unlike Cu and Pb, there is no sulphide control over the partitioning of Ga and Zn.

Figures 9 through **12** show considerable scatter in the diagrams of the Cu, Zn, Pb, and Ga versus MgO contents. We discuss below the nature of this scatter in relation to different petrogenetic factors. The abundance of an element in a primary, mantle-derived melt depends on the concentration of the given element in the mantle source region, the nature of the solid phases existing before and during melting, the partition coefficients, and the degree of partial melting. Further, the behavior (as to depletion or enrichment) of an element in the melt during subsequent fractional crystallization depends on the bulk distribution of that element. In **Figure 13** we have replotted all the modern oceanic crustal and ophiolitic mafic rocks (all undifferentiated), and we have superimposed fractional crystallization lines on this plot.

8.1.2. Partial melting and fractional crystallization models

Major element chemistry of the basaltic melts and phase proportions were modelled using pMELTS (Ghiorso et al., 2002). For the initial concentration of trace elements, we used instantaneous concentrations of Cu, Pb, Ga and Zn in basaltic melts during 5 and 10% fractional melting of a depleted mantle (DM) source following the same protocol as described in Kiseeva et al. (2017). Partition coefficients into the silicate minerals and element concentrations in the depleted mantle that we have used for modelling are shown in **Table 1**.

Sulphide was ignored in modelling Zn and Ga behaviour because it exerts no control over the concentrations of these elements in the liquid due to their low partition coefficients (~2.5 for Zn and ~0.03 for Ga). Produced by partial melting of a depleted mantle, 5 and 10% melts were then allowed to fractionally crystallize using Petrolog3 (Danyushevsky and Plechov, 2011). The starting liquid was nominally anhydrous and contained ~10.3 – 10.7 wt.%

MgO. Fe^{3+} was calculated using QFM buffer, and the pressure was kept constant at 8 kbar. The modelling was conducted with approximately 1% of melting interval and was stopped when ~20-25% melt was remained. At this point the MgO content of the melt was 2.5 – 2.7 wt.%. For the 5% melting of depleted mantle, Petrolog3 generated the following crystallization sequence: olivine, plagioclase, orthopyroxene and clinopyroxene. For the 10% melting of depleted mantle, olivine did not crystallize and clinopyroxene was on the liquidus followed by plagioclase and then orthopyroxene. Despite differences in the crystallization sequence, the produced curves for the starting composition of 5% and 10% melting of depleted mantle for both Zn and Ga were almost identical (**Fig. 13**). This phenomenon can probably be explained by very small proportions of olivine being crystallized (X = 0.03) before the crystallization of the other mineral phases.

In order to model high-Mg boninitic magmas, we used a hydrous W3.31 starting composition reported by Parman and Grove (2004) that contained 17.3 wt% MgO and 7.43 wt% H_2O, and fractionally crystallized at 10 kbars. For W3.31, Petrolog3 generated the following crystallization sequence: olivine, orthopyroxene, plagioclase and clinopyroxene. The melting was stopped when~11% of melt remained and with ~1 wt% of MgO remaining in the melt.

The behaviour of Pb and Cu is controlled largely by sulphide minerals rather than silicates; so, we did the Pb and Cu modelling by using the same liquid line of descent as for Zn and Ga, but by adding sulphide to the crystallization sequence. The partition coefficients for Cu and Pb into sulphide phases were calculated based on Kiseeva and Wood (2013, 2015). We used 900 ppm as initial sulphur concentration in the system, and the method of Smythe et al. (2017) to calculate the sulphur solubility. For the melt generated by 5% partial melting of the depleted mantle, the sulphide started precipitating when about 92% of melt was present in the system; for the W3.31 composition, the precipitation of sulphide started when ~85% melt was present in the system. Crystallization curves were generated for the initial amount of Pb in the system between 0.24 and 0.75 ppm, and for Cu between 80 and 120 ppm. These values are in a good agreement with the calculated amounts of Cu (116 ppm) and Pb (0.24 ppm) in the melt produced by 5% melting of the depleted mantle.

8.2. Crustal contamination effects

551

552 During the initial continental rifting phase, decompression melting of the sub-
553 continental mantle produces basaltic melts, which commonly become contaminated by the
554 ambient rock components on their ascent through the continental crust within the rift zone.
555 The continental crust varies in thickness between 30 to 60 km and is divided into upper,
556 middle, and lower parts (e.g., Gao, 2010). The upper crust consists of a variety of
557 sedimentary and igneous rocks, whereas the middle and lower continental crust is largely
558 dominated by high-grade metamorphic rocks with intermediate to felsic compositions. The
559 Cu, Zn, Pb and Ga contents are highly variable in the upper crust and show considerably
560 higher values in sedimentary rocks than in dioritic to granitic rocks (Hu and Gao, 2008).
561 Recommended values for Cu, Zn, Pb and Ga for the bulk crust are 27, 72, 11, and 16 ppm,
562 respectively (Rudnick and Gao, 2003), and these values are all within those of the compiled
563 data for the given elements (see **Figs. 3-6**). They are also comparable to the average values
564 of Zn and Ga in ophiolites (**Figs. 4 and 6**) but are somewhat lower than the average value for
565 Cu and much higher than the average value of Pb.
566 Thus, the Zn and Ga histogram patterns (**Figs. 4 and 6**, respectively) would largely
567 remain unchanged even if the ascending basaltic magmas of rift zones were contaminated by
568 continental crust. Pb contents, on the other hand, might be significantly affected, and we see
569 ample evidence to this effect in the histogram pattern (**Fig. 5**). This is particularly evident for
570 the Rift and Continental Margin, and the Volcanic Arc type ophiolites (**Fig. 5 B and F**,
571 respectively). Basaltic magmas of these ophiolite types ascended through continental crust,
572 and might thus have been contaminated, to varying extent, by Pb-enrichment (as well as other
573 elements such as Th). It is difficult to evaluate, based on the nature of the Cu histogram (**Fig.**
574 **3**), whether or not Cu values are affected by crustal contamination.
575

576 ***8.3. Subduction-related factors***

577

578 For the subduction-related ophiolite types, there are many factors related to the
579 dynamics of a subducting slab that may contribute to different element enrichment of the
580 basaltic melt. We consider below only the chalcophile elements of Cu, Zn and Pb, but we do

not consider the element Ga further because of the scarcity of the literature data. It is beyond the scope of this study to constrain the significance of subduction – related factors in the distribution patterns of chalcophile elements. However, we discuss here the four most salient factors based on the presently available data. These factors include: (1) subducted sediments; (2) subduction rates; (3) thermal structure; and (4) slab-water flux and released fluids.

8.3.a. Sedimentary cover

The sedimentary cover of a subducting slab and its Cu, Zn, and Pb contents may play an important role in variable enrichment of the basaltic melt. A comprehensive review of various parameters related to subduction zones is provided by Plank and Langmuir (1999). The sedimentary cover of an oceanic lithosphere subducted at trenches consists mainly of siliceous or carbonaceous ooze, clay, turbidites (silt/sand), and volcaniclastic material. These sediment types may appear in highly different proportions in different subduction systems and may also differ by one or two orders of magnitude with respect to their chalcophile element contents Cu: 27-317 ppm (av. 108); Zn: 25-243 ppm (av. 91); Pb: 1-113 ppm (av. 28). The average Cu content of 108 ppm of subducting sediments is higher than that of the average Cu contents of the various ophiolite types (**Fig. 3**), and hence these sediments should play some role in the enrichment of basaltic magmas in Cu. The average value of Zn (91 ppm) contents in subducted sediments, on the other hand, is comparable to most of the ophiolite types (**Fig. 4**) and is thus unlikely to play any significant role in their melt evolution. However, the average Pb content (28 ppm) in oceanic sediments is much higher than that of any of the ophiolite types (**Fig. 5**) and may, thus, have a profound influence on the Pb-content of the basaltic magmas in the melt column within the mantle wedge, following their subduction and subsequent melting.

8.3.b. Subduction rate

The subduction rate controls the amount of sediment per time unit that is carried down in a slab within a subduction zone (e.g., Scholl and van Huene; Safonova et al. 2015), and varies from ca. 1.5 cm/year to 16 cm/year (Plank and Langmuir, 1999; Hoareau et al., 2015). Thus, the amounts of sediments and the chalcophile elements that are carried down in a

subduction zone may vary profoundly with respect to subduction rates, and may, therefore, contribute to varying chemical fingerprints of SSZ oceanic crust and ophiolite types.

8.3.c. Thermal structure of a subduction zone

The third factor is the thermal structure of a subduction zone (van Keken, 2003; van Keken et al., 2011) that affects the areal extent and magnitude of slab dehydration. Mineralogically-bound water molecules in oceanic crustal rocks might be little disturbed with further and deeper slab descent of an old oceanic lithosphere, subducting at fast rates. However, subduction of a young and hydrated slab, taking place in hot and young convergent margins with slow subduction rates may result in its efficient dehydration and in significant amounts of fluids and melts released into the mantle wedge (van Keken et al., 2011).

8.3.d. Fluid flux derived from subducting slabs

Fluid flux derived from subducting slabs plays an important role in the enrichment of magmas in many trace elements (e.g., Wang and Xiao, 2018). It is a common knowledge that large – ion lithophile elements (LILEs) are mobilized during fluid-rock interactions, and that they lead to the enrichment of the upper mantle peridotites in the wedge above a subducting slab (e.g., Pearce and Parkinson, 1993; Pearce and Peate, 1995; Macdonald et al., 2000; Elburg et al., 2002). Chemical fingerprints of magmas and their products commonly reflect the nature of such slab – derived enrichments in the mantle melt source (Dilek and Furnes, 2009). Additionally, the chalcophile elements of Cu, Zn, and particularly Pb, are also fluid-transported from a subducting slab into the overlying mantle wedge (Kogiso et al., 1997; Li et al., 2013), and hence get incorporated into the melt column during the evolution of magmas. The solubility of these elements (particularly Cu) is determined by several factors, such as the abundance of S and Cl, and the HCl/alkali chloride ratio (Zajacz et al., 2011, 2017).

These discussions show that the number of variables is too high to make real quantifications about the contributions of various subduction-related processes to the contents and patterns of the chalcophile elements of Cu, Zn and Pb (**Figs. 3-5, 7, 8**) during the melt evolution of ophiolites. However, our analysis of the available data in the previous

643 sections indicate that the mantle melt sources of many ophiolites were significantly enriched
644 in Cu and Pb by one or a combination of the several factors discussed above.

645

646 ***8.4. Effects of primary and secondary factors***

647

648 We have briefly discussed the mobility behavior of the chalcophile elements,
649 and have explained that Cu and Zn (to a lesser extent) suffer loss during alteration and
650 low-grade metamorphism, whereas Pb becomes enriched as seen in **Fig. 13A, B and C**.
651 We have also defined the fields occupied by these elements with respect to the various
652 basaltic rocks of in-situ oceanic crust and ophiolites (alkaline basalt, MORB, IAT, and
653 boninites) (**Figs. 9-12**). These diagrams indicate a general trend of the lower contents of
654 these elements, particularly for Cu and Zn, in IAT and boninites in comparison to
655 MORB. The petrogenetic modelling indicates that much of the scatter in the Bowen
656 diagrams can be explained by 5-10 percent partial melting of a depleted mantle with
657 different starting concentrations, followed by 20-80% fractional crystallization as shown
658 in **Fig. 13A-D**.

659 The first question related to the nature of the Cu-histogram patterns of the various
660 ophiolite types **(Fig. 3)** is whether the Cu-depletion, as caused by alteration and
661 metamorphism, can be regarded as the main responsible process. All the ophiolites, regardless
662 of their geochemical affinity, display similar alteration mineral assemblages and textures
663 indicating that they underwent low-grade greenschist metamorphism and seafloor alteration
664 (see Figs. 17 and 24 in Furnes and Safonova, 2019; and Furnes et al., 2020, respectively), and
665 that they thus experienced nearly the same alteration and metamorphic processes subsequent
666 to their magmatic construction. On this basis, we consider the effects of seafloor alteration and
667 hydrothermal metamorphism as largely unlikely to account for the profound differences in the
668 documented Cu and Pb patterns in the crustal rocks of ophiolites (**Figs. 3 and 5**, respectively).
669 Therefore, we posit that the histogram patterns of the given chalcophile elements reflect
670 mainly petrogenetic processes involved in the magmatic evolution of ophiolites and oceanic
671 crust. Metamorphism and alteration, as well as some element exchange, for example Pb
672 enrichment by crustal contamination for the subduction-unrelated R/CM/P ophiolites, and by

673 one or several subduction-related processes for the subduction-related ophiolites, may play
674 some role. However, we ascribe the main controlling factors on the histogram patterns in **Figs.**
675 **9-12** to three main phenomena: (1) chalcophile element abundances in the mantle melt source;
676 (2) repeated partial melting episodes; and (3) fractional crystallization processes.
677
678 **9. Summary and Conclusions**
679
680 In this study we have investigated the distribution of chalcophile elements (mainly Cu,
681 Zn, Pb, and Ga) in the crustal and upper mantle rocks of the Phanerozoic ophiolites and
682 Precambrian greenstone belts based on the extant data in the literature. We have also evaluated
683 the nature of the geological processes, which had significant control on this elemental
684 distribution and related mineralization in the ancient oceanic lithosphere. Our results indicate
685 that the compositional distribution of Cu and Pb in different ophiolite types (subduction –
686 unrelated versus subduction – related) display significant variations, independently of their
687 hydrothermal alteration and low – temperature metamorphic histories. The compositional
688 distribution of Zn and Ga, on the other hand, show subtle variations in different ophiolites.
689 These observations imply that the mantle melt sources, melt evolution patterns and
690 metasomatic processes, and crustal contamination effects in different tectonic settings played a
691 major role in the enrichment of Cu and Pb concentrations in magmas and in related
692 mineralization during oceanic crust – ophiolite formation. Cu distribution and mineralization is
693 significant in MOR and backarc ophiolites but limited in forearc and volcanic arc ophiolites.
694 Pb distribution trends in ophiolites display progressively increasing low concentrations from
695 alkaline basalts and MORB affinities (subduction – unrelated) to IAT and boninitic affinities
696 (subduction – related).
697 The large scatter in MgO versus Cu, Zn, Pb, and Ga distribution in ophiolites and
698 modern oceanic crust, as displayed by our petrogenetic modelling results, is likely a
699 manifestation of fractional crystallization of melts, produced by 5% to 10% partial melting of
700 variously depleted mantle sources. The Cu and Pb behaviour during fractional crystallization is
701 controlled by sulphide minerals, instead of silicates. Pb concentrations in subduction –
702 unrelated ophiolitic magmas appear to have been affected significantly by crustal
703 contamination during melt ascent beneath rift zones, whereas Cu concentrations do not display

any related patterns hinting crustal contamination effects. The types and amounts of subducted sediments, the subduction rates, the thermal structure of a subduction zone, and the extent and chemistry of slab – released fluids at convergent zones strongly affected Cu and Pb enrichments in the melt column within the mantle wedge during the formation of subduction – related ophiolites. These findings suggest that chalcophile element distributions in ancient oceanic lithosphere can be used effectively as an additional geochemical tool to differentiate different ophiolite types in orogenic belts.

Acknowledegments

We thank Vasiliy Belyaev, Weiliang Liu, Franco Pirajno, Reimar Seltmann, Elham Bahramnejad for help in providing the relevant literature on mineralized ophiolites. We have interacted with and had numerous discussions with many colleagues in the international ophiolite community during our fieldwork and research in different orogenic belts and in Precambrian greenstone belts around the globe over the years; it is impossible to name all of them here, but we gratefully acknowledge all those fruitful outcrop discussions and significant insights we have received. We thank Duane Smythe for advice on modelling and its interpretation, and Editor Graham Shields for inviting this submission as a Review Paper to the *Journal*.

725 **References**

726

727 Acharya, S. 2013. Lead between the lines. *Nature Chemistry*, **5**, 895,
728 https://doi.org/10.1038/nchem.1761.
729 Aftabi, A., Ghodrati, Z. & MacLean, W.H. 2006. Metamorphic textures and geochemistry of
730 the Cyprus-type massive sulfide lenss at Zurbad, Knoy, Iran. *Journal of Asian Earth*
731 *Sciences*, **27**, 523-533.
732 Alt, J.C. 1995. Subseafloor processes in mid-ocean ridge hydrothermal systems. In: Seafloor
733 Hydrothermal Systems, Physical, Chemical, Biological, and Geological Interactions
734 (eds. Humphris, S.E., Zierenberg, R.A., Mullineaux, L.S., Thomson, R.E. Geophysical
735 Monograph, vol. 91, pp. 85-114. American Geophysical Union, Washington DC.
736 Alt, J.C., Laverne, C., Coggon, R.M., Teagle, D.A.H., Banerjee, N.R., Morgan, S., Smith-
737 Duque, C.E., Harris, M. & Galli, L. 2010. Subsurface structure of a submarine
738 hydrothermal system in the ocean crust formed at the East Pacific Rise, ODP/IODP Site
739 1256. *Geochemistry Geophysics Geosystems*, **11** (10), Q10010,
740 doi:10.1029/2010GC003144.

741 Anonymous, 1972. Penrose field conference on ophiolites. *Geotimes*, **17**, 24-25.

742 Antivachis, D.N. 2015. The geology of the northern part of the Apilki Cyprus-type ore deposit.
743 *Bulletin of the Geological Society of Greece*, **XLIX**, 4-28.

744 Balestro, G., Festa, A. & Dilek, Y. 2019, Structural Architecture and Extensional Tectonics of
745 the Western Alpine Ophiolites, and Pre-collisional Reconstruction of the Jurassic Alpine
746 Tethys. *Journal of the Geological Society of London*, **176** (5), 913-930, doi:
747 10.1144/jgs2018-099.

748 Bédard, J.H. 2006. Trace element partitioning in plagioclase feldspar. *Geochimica*
749 *et Cosmochimica Acta*, **70**, 3717-3742.
750 Brenner, A.R., Fu, R.R., Evans, D.A., Smirnov, A.V., Trubko, R. & Rose, I.R. 2020.
751 Paleomagnetic evidence for modern-like plate motion velocities at 3.2 Ga. *Science*
752 *Advances*, **6 eaaz8670**.
753 Condie, K.C. 2018. A planet in transition: The onset of plate tectonics on Earth between 3 and

754 2 Ga? *Geoscience Frontiers*, **9**, 51-60.
755 Craw, D., Williams, J.G. & Johnstone, R.D. 1997. Regional metamorphic Cu mobilization in
756 calc- alkaline rocks, Eglinton valley, Southland, New Zealand. *New Zealand Journal of*
757 *Geology and Geophysics*, **40**, 31-41.
758 Danyushevsky, L.V. & Plechov, P. 2011. Petrolog3: Integrated software for modelling
759 crystallization processes. *Geochemistry Geophysics Geosystems*, **12** (7), Q07021.
760 Davis, F.A., Humayun, M., Hirschmann, M.M. & Cooper, R.S. 2013. Experimentally
761 determined mineral/melt partitioning of first-row transition elements (FRTE) during
762 partial melting of peridotite at 3 GPa. *Geochimica et Cosmochimica Acta*, **104**, 232-
763 260.
764 Dewey, J.F., Kiseeva, E.S., Pearce, J.A. & Robb, L.J. 2021. Precambrian tectonic evolution of
765 Earth: an outline. *South African Journal of Geology*, **124** (1), 141 – 162.
766 doi:10.25131/sajg.124.0019.
767 De Wit, M.J., Furnes, H. & Robins, B. 2011. Geology and tectonostratigraphy of the Onverwacht
768 Suite, Barberton Greenstone Belt, South Africa. *Precambrian Research* **186**, 1-27.
769 De Wit, M., Furnes, H., MacLennan, S., Doucoure, M., Schoene, B., Weckmann, U., Martinez, U.
770 & Bowring, S. 2018. Paleoarchean bedrock litholgies across the Makhonjwa Mountains of
771 South Africa and Swaziland linked to geochemical, magnetic and tectonic data reveal early
772 plate tectonic genes flanking subduction margins. *Geoscience Frontiers*, **9**, 603-665.
773 Dhuime, B., Wuestefeld, A. & Hawkesworth, C.J. 2015. Emergence of modern continentral
774 crust about 3 billion years ago. *Nature Geoscience*, **8**, 552-556.
775 Dilek, Y. 1989a. Tectonic significance of post-accretion rifting of a Mesozoic island-arc terrane
776 in the northern Sierra Nevada, California. *Journal of Geology*, **97**, 503-518.
777 Dilek, Y. 1989b. Structure and tectonics of an Early Mesozoic oceanic basement in the northern
778 Sierra Nevada metamorphic belt, California: Evidence for transform faulting and ensimatic
779 arc evolution. *Tectonics*, **8**, 999-1014. doi: 10.1029/TC008i005p0999.
780 Dilek, Y. & Eddy, C.A. 1992. The Troodos (Cyprus) and Kizildag (S. Turkey) ophiolites as
781 structural models for slow-spreading ridge segments. *Journal of Geology*, **100** (3), 305-322.
782 Dilek, Y. & Thy, P. 1998. Structure, petrology, and seafloor spreading tectonics of the Kizildag
783 ophiolite (Turkey). In, R. Mills and K. Harrison (Eds.), Modern Ocean Floor Processes and
784 the Geological Record, *Geological Society of London Special Publication*,**148**, 43-69.

785 Dilek, Y. & Flower, M.F.J. 2003. Arc-trench rollback and forearc accretion: 2. Model template
786 for Albania, Cyprus and Oman: In, Dilek, Y. & Robinson, P.T. (Eds.), Ophiolites in Earth
787 History, *Geological Society of London Special Publication*, **218**, 43-68.
788 Dilek, Y. & Furnes, H. 2009. Structure and geochemistry of Tethyan ophiolites and their
789 petrogenesis in subduction rollback systems. *Lithos*, **13** (1-2), 1-20. doi:
790 10.1016/j.lithos.2009.04.022.
791 Dilek, Y. & Furnes, H. 2011. Ophiolite genesis and global tectonics: Geochemical and tectonic
792 fingerprinting of ancient oceanic lithosphere. *Geological Society of America Bulletin*, 123
793 (3/4), 387-411. Doi: 10.1130/B30446.1.
794 Dilek, Y. & Furnes, H. 2014. Ophiolites and their origins. *Elements*, **10**, 93-100.
795 Dilek, Y. & Thy, P. 2009. Island arc tholeiite to boninitic melt evolution of the Cretaceous
796 Kizildag (Turkey) ophiolite: model for multi-stage early arc–forearc magmatism in
797 Tethyan subduction factories. *Lithos*, **113** (1-2), 68-87.
798 Dilek, Y., Furnes, H. & Skjerlie, K.P. 1997. Propagating rift tectonics of a Caledonian marginal
799 basin: Multi-stage seafloor spreading history of the Solund-Stavfjord ophiolite in western
800 Norway. *Tectonophysics*, **280** (3-4), 213-238.
801 Dilek, Y., Moores, E.M. & Furnes, H. 1998. Structure of modern oceanic crust and ophiolites
802 and implications for faulting and magmatism at oceanic spreading centers. In, R. Buck, J.
803 Karson, P. Delaney and Y. Lagabrielle (Eds.), Faulting and Magmatism at Mid-Ocean
804 Ridges, *American Geophysical Union Monograph*, **106**, 219-266.
805 Dilek, Y., Shallo, M. & Furnes, H. 2005. Rift-drift spreading and subduction zone tectonics of
806 Albanian ophiolites. *International Geology Review*, **47**, 147-176, doi:
807 10.2747/00206814.47.2.147.
808 Eason, D.E. & Dunn, R.A. 2015. Petrogenesis and structure of oceanic crust in the Lau back-arc
809 basin. *Earth and Planetary Science Letters*, **429**, 128 – 138.
810 Eddy, C.A., Dilek, Y., Hurst, S. & Moores, E.M. 1998. Seamount formation and associated
811 caldera complex and hydrothermal mineralization in ancient oceanic crust. Troodos
812 Ophiolite (Cyprus). *Tectonophysics*, **292** (3-4), 189-210.
813 Elburg, M.A., van Bergen, M., Hoogewerfe, J., Foden, J., Vroon, P., Zulkarnain, I. &

814 Nasution, A. 2002. Geochemical trends across an arc-continent collision zone: magma
815 sources and slab- wedge transfer processes below the Pantar Strait volcanoes, Indonesia.
816 *Geochimica et Cosmochimica Acta*, **66**, 2771-2789.

817 Foley, S.F., Prelevic, D., Rehfeldt, T. & Jacob, D.E. 2013. Minor and trace elements in
818 olivines as probes into early igneous and mantle melting processes. *Earth and Planetary*
819 *Science Letters*, **363**, 181-191.

820 Fowler, A.P.G. & Zierenberg, R.A. 2016. Elemental changes and alteration recorded by
821 basaltic drill core samples recovered from in situ temperatures up to 345 C in the active,
822 seawater- recharged Reykjanes geothermal system, Iceland. *Geochemistry Geophysics*
823 *Geosystems*, **17**, doi.10.1002/2016GC006595.

824 Furnes, H. & Dilek, Y. 2017. Geochemical characterization and petrogenesis of
825 intermediate to silicic rocks in ophiolites: A global synthesis. *Earth-Science Reviews*,
826 **166**, 1-37.

827 Furnes, H. & Safonova, I. 2019. Ophiolites of the Central Asian Orogenic Belt: Geochemical
828 and petrological characterization and tectonic settings. *Geoscience Frontiers*, **10**, 1255-
829 1284.

830 Furnes, H., Robins, B. & de Wit, M.J. 2012. Geochemistry and petrology of lavas in the upper
831 Onverwacht Suite, Barberton Mountain Land, South Africa. *South African Journal of*
832 *Geology*, **115.2**, 171-210.

833 Furnes, H., de Wit, M., Staudigel, H., Rosing, M. & Muehlenbachs, K. 2007. A vestige of
834 Earth's oldest ophiolite. *Science*, **315**, 1704-1707.

835 Furnes, H., Rosing, M., Dilek, Y. & de Wit, M. 2009. Isua supracrustal belt (Greenland) – A
836 vestige of ca. 3.8 Ga suprasubduction ophiolite, and the implications for Archean
837 geology. *Lithos*, **113**, 115-132.

838 Furnes, H., de Wit, M. & Dilek, Y. 2014. Four billion years of ophiolites reveal secular trends
839 in oceanic crust formation. *Geoscience Frontiers*, **5**, 571-603.

840 Furnes, H., Dilek, Y. & de Wit, M. 2015. Precambrian greenstone sequences represent different
841 ophiolite types. *Gondwana Research*, **27**, 649-685.

842 Furnes, H., Dilek, Y., Zhao, G., Safonova, I. & Santosh, M. 2020. Geochemical characterization of
843 ophiolites in the Alpine-Himalayan Orogenic Belt: Magmatically and tectonically diverse
844 evolution of the Mesozoic Neotethyan oceanic crust. *Earth-Science Reviews*, **208**, 103258.

845 Galley, A.G. & Koski, R.A. 1999. Setting and characteristics of ophiolite-hosted
846 volcanogenic massive sulfide deposits. *Reviews Economic Geology*, **8**, 221-246.
847 Galley, A.G., Hannington, M.D. & Jonasson, I.R. 2007. Volcanogenic massive sulphide
848 deposits: *Geological Association of Canada, Mineral Deposits Division, Special*
849 *Publication*, **5**, 141–161.
850 Gao, S. 2010. Chemical composition of the continental crust: a perspective from China.
851 Geochemical News, **142**, 1-15.
852 Ghiorso, M.S., Hirschmann, M.M., Reiners, P.W. & Kress, V.C. 2002. The pMELTS: A
853 revision of MELTS for improved calculatiton of phase relations and major element
854 partitioning related to partial melting of mantle at 3 GPa. *Geochemistry Geophysics*
855 *Geosystems*, **3** (5), 1-35.
856 Gillis, K.M. & Thompson, G. 1993. Metabasalts from the Mid-Atlantic Ridge: new insights
857 into hydrothermal systems in slow-spreading crust. *Contributions to Mineralogy and*
858 *Petrology*, **113**, 502-523.
859 Godfrey, N.J. & Dilek, Y. 2000. Assimilation of oceanic crust/island arc into the north American
860 continental margin: New insights from geophysical data: In, Dilek, Y., Moores, E.M., Elthon,
861 D. & Nicolas, A. (Eds.), Ophiolites and Oceanic Crust: New Insights from Field Studies and
862 Ocean Drilling Program, *Geological Society of America Special Paper*, **349**, 371-387.
863 Goldschmidt, V.M. 1937. The principles of distribution of chemical elements in minerals and rocks.
864 The seventh Hugo Müller Lecture, delivered before the Chemical Society on March 17th,
865 1937. *Journal of the Chemical Society (Resumed),* 655-673.
866 Gregory, M.J. 2006. Copper mobility in the Eastern Creek Volcanics, Mount Isa, Australia:
867 evidence from the laser ablation ICP-MS of iron-titanium oxides. *Mineralium Deposita*,
868 **41**, 691-711.
869 Grønlie, G. & Logn, Ø. 1978. The Old Vigsnes copper mine at Karmøy, western Norway.
870 Presentation of geophysical data. *Norsk Geologisk Tidsskrift*, **58**, 81-91.
871 Hamilton, W.B. 2011. Plate tectonics began in Neoproterozoic time. And plumes from
872 deep mantle have never operated. *Lithos*, **123**, 1-20.
873 Hannington, A.D., Galley, A.G., Herzig, P.M. & Petersen, S. 1998. Comparison of the TAG
874 mound and stockwork complex with Cyprus-type massive sulphide deposits.

Proceedings of the Ocean Drilling Program, Scientific Results, **158**, 389-415.

Hart, S.R., Erlank, A.J. & Kable, E.J.D. 1974. Sea floor basalt alteration: Some chemical and Sr isotopic effects. *Contributions to Mineralogy and Petrology*, 44, 219-230.

Hein, R.J. & Mizell, K. 2013. Hydrothermal systems and mineralization of volcanic arcs: Comparison of West Pacific and Mediterranean arc. In: Proceedings of the Summer training school "Geological setting, Mineral Resources and ancient works of Samos and adjacent islands of the Aegean Sea", 26-30 August 2013, Karlovassi, Samos Island, Greece.

Hoareau, G., Bomou, B., van Hinsbergen, D.J.J., Carry, N., Marquer, D., Donnadieu, Y., Le Hir, G., Vrielynck, B. & Walter-Simonnet, A.-V. 2015. Did high Neo-Tethyan subduction rates contribute to early Cenozoic warming? Climate of the Past, **11**, 1751-1767.

Hopkins, M.D., Harrison, T.M. & Manning, C.E. 2008. Low heat flow inferred from > 4 Gyr zircons suggests Hadean plate boundary interactions. *Nature*, **456**, 493-496.

Hu, Z. & Gao, S. 2008. Upper crustal abundances of trace elements: A revision and update. *Chemical Geology*, **253**, 205-221.

Jenner, F.E., Hauri, E.H., Bullock, E.S., König, S., Arculus, R.J., Mavrogenes, J.A., Mikkelson, N. & Goddard, C. 2015. The competing effects of sulfide saturation versus degassing on the behavior of the chalcophile elements during the differentiation of hydrous melts. *Geochemistry Geophysics Geosystems*, **16**, 1490-1507.

Jowitt, S.M., Jenkin, G.R.T., Coogan, L.A. & Naden, L. 2012. Quantifying the release of base metals from source rocks for volcanogenic massive sulfide deposits: Effects of protolith composition and alteration mineralogy. *Journal of Geochemical Exploration*, **118**, 47-59.

Kato, C. & Moynier, F. 2017. Gallium isotopic evidence for extensive volatile loss from the Moon during its formation. *Science Advances*, **3**, e1700571.

Kato, T. Beavan, J., Matsushima, T., Kotake, Y., Juan T. Camach, J.T. & Nakao, S. 2003. Geodetic evidence of back-arc spreading in the Mariana Trough. *Geophysical Research Letters*, **30** (12), 1625, doi:10.1029/2002GL016757.

Kogiso, T., Tatsumi, Y. & Nakano, S. 1997. Trace element transport during dehydration processes in the subducted oceanic crust: 1. Experiments and implications for the origin of ocean island basalt. *Earth and Planetary Science Letters*, **148**, 193-205.

Kiseeva, E.K. & Wood, B.J. 2013. A simple model for chalcophile element partitioning

between sulphide and silicate liquids with geochemical applications. *Earth and Planetary Science Letters*, **383**, 68- 81.

Kiseeva, E.K. & Wood, B.J. 2015. The effects of composition and temperature on chalcophile and lithophile element partitioning into magmatic sulphides. *Earth and Planetary Science Letters*, **424**, 280- 294.

Kiseeva, E.S., Fonseca, R.O.C. & Smythe, D.J. 2017. Chalcophile Elements and Sulfides in the Upper Mantle. *Elements*, **13**, 111-116.

Le Roux, V., Dasgupta, R. & Lee, C.T.A. 2015. Recommended mineral-melt partition coefficients for FRTEs (Cu), Ga, and Ge during mantle melting. *American Mineralogist*, **100**, 2533- 2544.

Li, J-L., Gao, J., John, T., Klemd, R. & Su, W. 2013. Fluid-mediated metal transport in subduction zones and its link to arc-related giant ore deposits: Constraints from a sulfide-bearing HP vein in lawsonite eclogite (Tianshan, China). *Geochimica et Cosmochimica Acta,* **120**, 326-362.

Macdonald, R., Hawkesworth, C.J. & Heath, E. 2000. The Lesser Antilles volcanic chain: a study in arc magmatism. *Earth-Science Reviews*, **49**, 1-76.

McDonough, W.F. & Sun, S.S. 1995. The composition of the Earth. *Chemical Geology*, **120**, 223-253.

Mahfoud, R.F. & Beck, J.N. 1997. Copper Mineralization in the Ophiolite of Oman: The Genesis and Emplacement Relationship with the Orogenic Movements of Serpentinized Peridotite. *International Geology Review*, **39**, 252-286.

Metz, S. & Trefry, J.H. 2000. Geochemical and mineralogical influences on concentrations of trace metals in hydrothermal fluids. *Geochimica et Cosmochimica Acta*, **64** (13), 2267-2279.

McQueen, K.G. 1990. The Dragset copper-zink deposit: a deformed, volcanogenic sulphide occurrence in the Løkken greenstones, Central Norway. *Norsk Geologisk Tidsskrift*, **70**, 1-19.

Milushi, I. 2015. An Overview of the Albanian Ophiolite and Related Ore Minerals. *Acta Geologica Sinica*, **89** (Supp. 2), 61-64.

Nakamura, K., Kato, Y., Tamaki, K. & Ishii, T. 2007. Geochemistry of hydrothermally altered basaltic rocks from the Southwest Indian Ridge near the Roderiguez Triple Junction. *Marine Geology*, **239**, 125-141.

Nutman, A.P., Bennett, V.C. & Friend, C.R.L., Rosing, M.T. 1997. ~3710 and ≥3790

937 Ma volcanic sequences in the Isua (Greenland) supracrustal belt; structural and
938 Nd isotope implications. *Chemical Geology*, **141** (3-4), 271-287.
939 Ordonez-Calderon, J.C., Polat, A., Fryer, B.J., Appel, P.W.U., van Gool, J.A.M., Dilek, Y, &
940 Gagnon, J. 2009. Geodynamic origin of dismembered fragments of Mesoarchean oceanic
941 crust in the Ujurassuit and Ivisaartoq greenstone belts, SW Greenland. *Lithos*, **113** (1-2),
942 133-157, doi: 10.1016/j.lithos.2008.11.005.
943 Palin, M.R. & Santosh, M. 2021. Plate tectonics: What, where, why, and when? *Gondwana*
944 *Research* (in press).
945 Palin, R.M., Santosh, M., Cao, W., Li, S., Hernandez-Uribe, D. & Parsons, A.J. 2020.
946 Secular change and the onset of plate tectonics on Earth. *Earth-Science Reviews*,
947 **207**, 103172. http://doi.org/10.1016/j.eascirev.2020.1034172.
948 Palme, H. & O'Neill, H. 2013. Cosmochemical Estimates of Mantle Composition,
949 Treatise on Geochemistry: Second Edition, pp. 1-39.
950 Paniello, R.C., Day, J.M.D. & Moynier, F. 2012. Zinc isotopic evidence for the origin of
951 the Moon. *Nature*, **490**, 376-380.
952 Paradis, S. 2015. Indium, germanium and gallium in volcanic- and sediment-hosted base-metal
953 sulphide deposits. In: Simandl, G.J. and Neetz., (Eds,). Symposium on Strategic and
954 Critical Materials Proceedings, November 13-14, 2015, Victoria, British Columbia.
955 British Columbia Ministry of Energy and Mines. British Columbia Geological Survey
956 Paper 2015-3, pp. 23-29.
957 Parman, S.W. & Grove, T.L. 2004. Harzburgite melting with and without H2O: Experimental data
958 and predictive modeling. *Journal of Geophysical Research Solid Earth*, **109** (B2).
959 Pearce, J.A. & Parkinson, I.J. 1993. Trace element models for mantle melting: application to
960 volcanic arc petrogenesis, In: Prichard, H.M., Alabaster, T., Harris, N.B.W., Neary, C.R.
961 (eds.), Magmatic Processes and Plate Tectonics. *Geological Society of London Special*
962 *Publication*, **76**, 373-476, 03.
963 Pearce, J.A. & Peate, D.W. 1995. Tectonic implications of the composition of volcanic arc
964 magmas. *Annual Reviews of Earth Planetary Sciences*, **23**, 251-285.
965 Pearce, J.A. 2014. Ophiolites: immobile elements fingerprinting of ophiolites. *Elements*, **10** (2),
966 101-108.
967 Phillips-Lander, C. & Dilek, Y. 2008. Structural architecture of the sheeted dike complex and

968 extensional tectonics of the Jurassic suprasubduction zone Mirdita ophiolite, Albania. *Lithos*,
969 **108**, 192-206. DOI: 10/1016/j.lithos.2008.09.014.
970 Pirajno, F., Uysal, I. & Naumov, E.A. 2020. Oceanic lithosphere and ophiolites: Birth. Life
971 and final resting place of related ore deposits. *Gondwana Research*, **88**, 333-352.
972 Plank, T. & Langmuir, C.H. 1999. The chemical composition of subducting sediment and
973 its consequences for the crust and mantle. *Chemical Geology*, **145**, 325-394.
974 Polat, A. Frei, R. Appel, P.W. U., Dilek, Y., Fryer, B., Ordnez-Calderon, J.C. & Yang, Z. 2007.
975 The origin and compositions of the Mesoarchean oceanic crust: Evidence from the 3075 Ma
976 Ivisaartoq greenstone belt, southern West Greenland. *Lithos*, **100**, 293-321. doi:
977 10.1016/j.lithos/2007.06.021.
978 Rudnick, R.L. & Gao, S. 2003. Composition of the Continental Crust. *Treatise on Geochemistry*,
979 **3**, 1-64.
980 Saalmann, K. & Laine, E.L. 2014. Structure of the Outokumpu ore district and ophiolite-
981 hosted Cu-Co-Zn-Ni-Ag-Au sulfide deposits revealed from 3D modeling and 2D high-
982 resolution seismic data. *Ore Geology Reviews*, **62**, 156-180.
983 Saccani, E. 2015. A new method of discriminating different types of post-Archean ophiolitic basalts
984 and their tectonic significance using Th-Nb and Ce-Dy-Yb systematics. *Geoscience Frontiers*,
985 **6**, 481-501.
986 Saccani, E., Dilek, Y., Marroni, M. & Pandolfi, L. 2015. Continental margin ophiolites of
987 Neotethys: Remnants of ancient ocean-continent transition zone (OCTZ) lithosphere and their
988 geochemistry, mantle sources and melt evolution patterns. *Episodes*, **38** (4), 230-249. doi:
989 10.18814/epiiugs/2015/v38i4/82418.
990 Safonova, I., Kojima, S., Nakae, S., Romer, R., Seltmasnn, R., Sano, H. & Onoue, T. 2015. Oceanic
991 island basalts in accretionary complexes of SW Japan: tectonic and petrogenetic implications.
992 *Journal of Asian Earth Sciences*, **113**, 508-523.
993 Sahlström, S., Arribas, A., Dirks, P., Corral, I. & Chang, Z. 2017. Mineralogical Distribution of
994 Germanium, Gallium and Indium at the Mt Carlton High-Suldidation Epithermal Deposit, NE
995 Australia, and Comparison with Similar Deposits Worldwide. *Minerals*, **7**, 213,
996 doi:10.3390/min7110213.
997 Savage, P.S., Moynier, F., Chen, H., Siebert, J., Badro, J., Puchtel, I.S. & Shofner, G. 2015.
998 Copper isotope evidence for large-scale sulphide fractionation during Earth's differentiation.

Geochemical Perspectives Letters, **1**, 53-64.

Scholl, D.W. & van Huene, R. 2007. Crustal recycling at modern subduction zones applied to the past – issues of growth and preservation of continental basement crust, mantle geochemistry, and supercontinent reconstruction. *Memoir of the Geological Society of America*, **200**, 9-32. https://doi.org/10.1130/2007.1200(02).

Smythe, D.J., Wood, B.J.& Kiseeva, E.S. 2017. The S content of silicate melts at sulfide saturation: New experiments and a model incorporating the effects of sulfide composition. A*merican Mineralogist*, **102** (4), 795-803.

Van Keken, P.E. 2003. The structure and dynamics of the mantle wedge. *Earth and Planetary Science Letters*, **215**, 323-338.

Van Keken, P.E., Hacker, B.R., Syracuse, E.M. & Abers, G.A. 2011. Subduction factory: 4. Depth-dependent flux of H2O from subducting slabs worldwide. *Journal of Geophysical Research*, **116**, B01401, doi:10.1029/2010JB007922.

Varnavas, S.P. & Papavasiliou, C. 2020. hydrothermal mineralization processes and insular mineralization in the Hellenic Volcanic Arc system: A review. *Ore Geology Reviews*, **124**, 103541.

Wang, Y-Y. & Xiao, Y. 2018. Fluid-controlled element transport and mineralization in subduction zones. *Solid Earth Sciences*, **3**, 87-104.

Wang, Z. & Becker, H. 2015. Abundances of Ag and Cu in mantle peridotites and the implications for the behavior of chalcophile elements in the mantle. *Geochimica et Cosmochimica Acta*, **160**, 209-226.

Windley, B.F., Kusky, T. & Polat, A. 2021. Onset of plate tectonics by the Eoarchean. Precambrian Research, 352, 105980.

Wyborn, L.A.I. 1987. The petrology and geochemistry of alteration assemblages in the Eastern Creek Volcanics, as a guide to copper and uranium mobility associated with regional metamorphism and deformation, Mount Isa, Queensland. In: Geochemistry and Mineralization of Proterozoic Volcanic Suites (eds. Pharaoh, T.C., Beckinsale, R.D., Rickard, D), *Geological Society Special Publication*, **33**, 425-434.

Xia, Y., Kiseeva, E.S., Wade, J. & Huang, F. 2019. The effect of core segregation on the Cu and Zn isotope composition of the silicate Moon. *Geochemical Perspectives Letters*, **12**, 12-17.

Yang, G.-X. & Dilek, Y. 2015. OIB- and P-Type Ophiolites Along the Yarlung-Zangbo Suture

Zone (YZSZ), Southern Tibet: Poly-Phase Melt History and Mantle Sources of the Neotethyan Oceanic Lithosphere. *Episodes*, **38** (4), 250-265. doi: 10.18814/epiiugs/2015/v39i4/82420.

Yu, M.-M., Dilek, Y., Yumul Jr, G.P., Yan, Y., Dimalanta, C.B. & Huang, C.-Y. 2020. Slab-controlled elemental-isotopic enrichments during subduction initiation magmatism and variations in forearc chemostratigraphy. *Earth and Planetary Science Letters*, **538**, 116217, https://doi.org/10.1016/j.epsl.2020.116217.

Zajacz, Z., Seo, J.H., Candela, P.A., Piccoli, P.M. & Tossell, J.A. 2011. The solubility of copper in high-temperature magmatic vapors: A quest for the significance of various chloride and sulfide complexes. *Geochimica et Cosmochimica Acta*, **75**, 2811-2827.

Zajacz, Z., Candela, P.A. & Piccoli, P.M. 2017. The partitioning of Cu, Au and Mo between liquid and vapor at magmatic temperatures and its implications for the genesis of magmatic-hydrothermal ore deposits. *Geochimica et Cosmochimica Acta*, **207**, 81-101.

Figure captions

Fig. 1. Schematic plate tectonic diagram illustrating the magmatic settings of oceanic lithosphere, and spatial tectonic setting, crustal architecture and lithology of the various ophiolite types. Modified from Dilek & Furnes (2011, 2014), Furnes & Dilek (2017), Furnes et al. (2020). Abbreviations and acronyms: DC=dike complex; IAT=island arc tholeiite; Bon.=boninite; And- lava=andesite lava; DA/Rhy=dacite/rhyolite; Gr/ton=granodiorite/tonalite; Gb=gabbro; CC=continental crust; VC=volcaniclastics; AWC=arc wedge corner; SDM=slab dehydration mantle; SMM=subduction-metasomatized mantle; MEM=moderately-enriched mantle; HEM=highly-enriched mantle.

Fig. 2. Templates for discrimination diagrams used for the geochemical determination of tectonic settings of formation of ophiolite types (modified after Pearce, 2014). (A) Nb/Yb – Th/Yb; and (B) Ti/1000 – V diagrams.

Fig. 3. Cu histograms for all the subduction-unrelated and subduction-related ophiolite types. Reference to data shown in Supplementary Table 1.

Fig. 4. Zn histograms for all the subduction-unrelated and subduction-related ophiolite types. Reference to data shown in Supplementary Table 1.

Fig. 5. Pb histograms for all the subduction-unrelated and subduction-related ophiolite types. Reference to data shown in Supplementary Table 1.

Fig. 6. Ga histograms for all the subduction-unrelated and subduction-related ophiolite types. Reference to data shown in Supplementary Table 1.

Fig. 7. Cu, Zn, Pb and Ga histograms showing the patterns of the different rock types (alkaline, MORB, IAT, boninite) of ophiolites. Reference to data shown in Supplementary Table 1.

Fig. 8. Cu, Zn, Pb and Ga histograms showing the patterns of different mantle lithologies. Reference to data applied is shown in Supplementary Table 2.

1074 **Fig. 9.** Cu-MgO relationships for A: Rocks from different in-situ oceanic environments
1075 (references to data in Supplementary Table 3), and B: different rocks from ophiolite
1076 complexes (reference to data in Supplementary Table 1).

1077 **Fig. 10.** Zn-MgO relationships for A: Rocks from different in-situ oceanic environments
1078 (references to data in Supplementary Table 3), and B: different rocks from ophiolite
1079 complexes (reference to data in Supplementary Table 1).

1080 **Fig. 11.** Pb-MgO relationships for A: Rocks from different in-situ oceanic environments
1081 (references to data in Supplementary Table 3), and B: different rocks from ophiolite
1082 complexes (reference to data in Supplementary Table 1).

1083 **Fig. 12.** Pb-MgO relationships for A: Rocks from different in-situ oceanic environments
1084 (references to data in Supplementary Table 3), and B: different rocks from ophiolite
1085 complexes (reference to data in Supplementary Table 1).

1086 **Fig. 13.** Cu-, Zn-, Pb-, and Ga-MgO for all ophiolites and in-situ oceanic crust, upon which
1087 various partial melting and factional crystallization lines are superimposed. In diagram A, the
1088 extent of fractional crystallization (20, 60 and 80%) is shown. Also, the most common
1089 alteration trends for Cu, Zn and Pb are indicated.

Click here to access/download;table;Table 1.xlsx

Table 1. Partition coefficients used for fractional melting and crystallization

	Olivine	Clinopyroxene	Orthopyroxene	Spinel	Plagioclase	Sulphide
Cu	0.05	0.043	0.15	0.22	0.005	200-830
Pb	0.003	0.1	0.009	0.001	0.5-0.75	7-26
Zn	0.96	0.333	0.451	5.2	0.1	2.5
Ga	0.026	0.357	0.3	6.5	1.060150376	0.03

Initial abundances in the Depleted Mantle (in ppm)

	Cu	Pb	Zn	Ga
Salters and Stracke, 2(	30	0.0232	56	3.2

Figure 1

Click here to access/download;figure;Fig. 01 Tectonic setting & Ophiolite types_.jpg

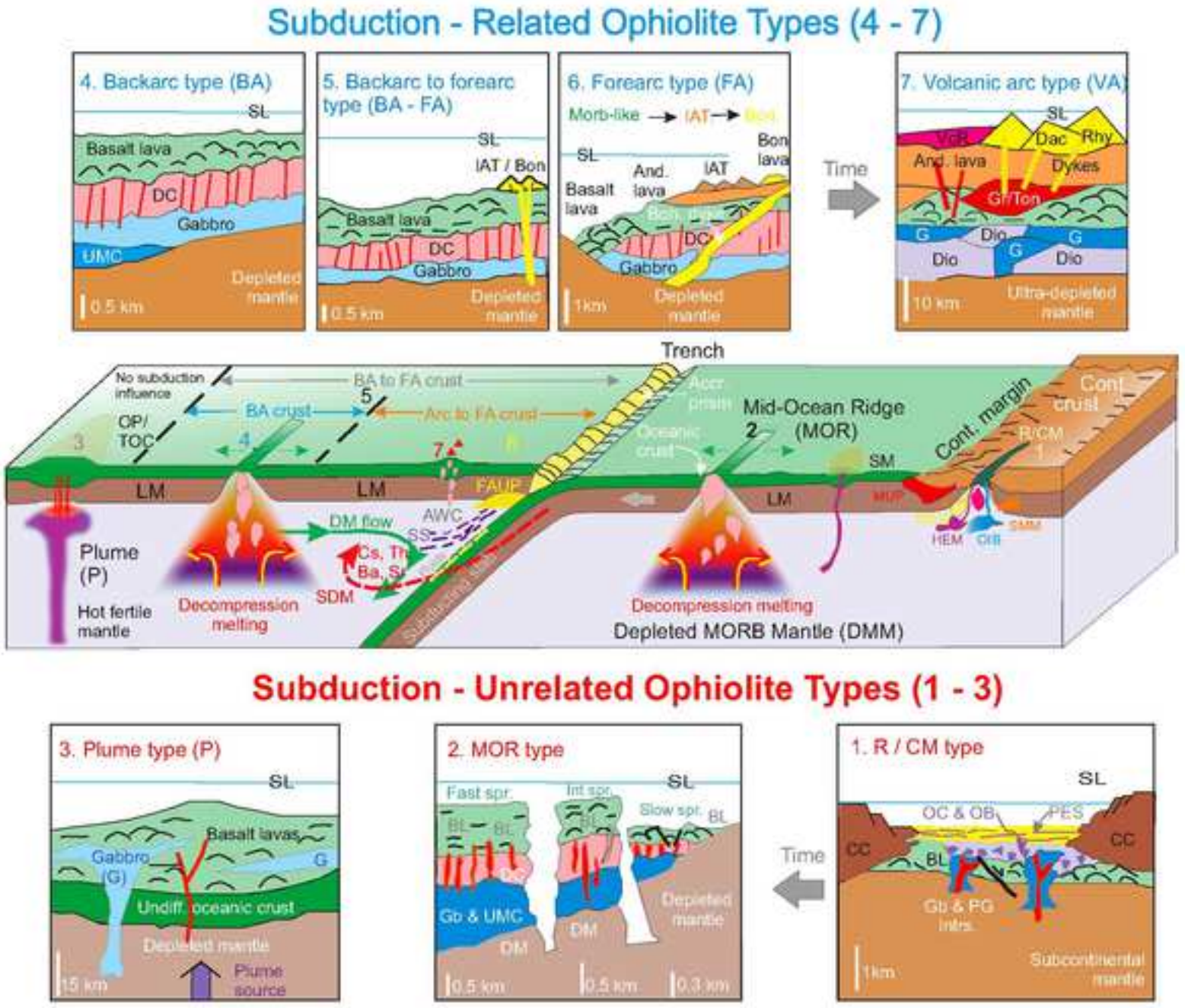
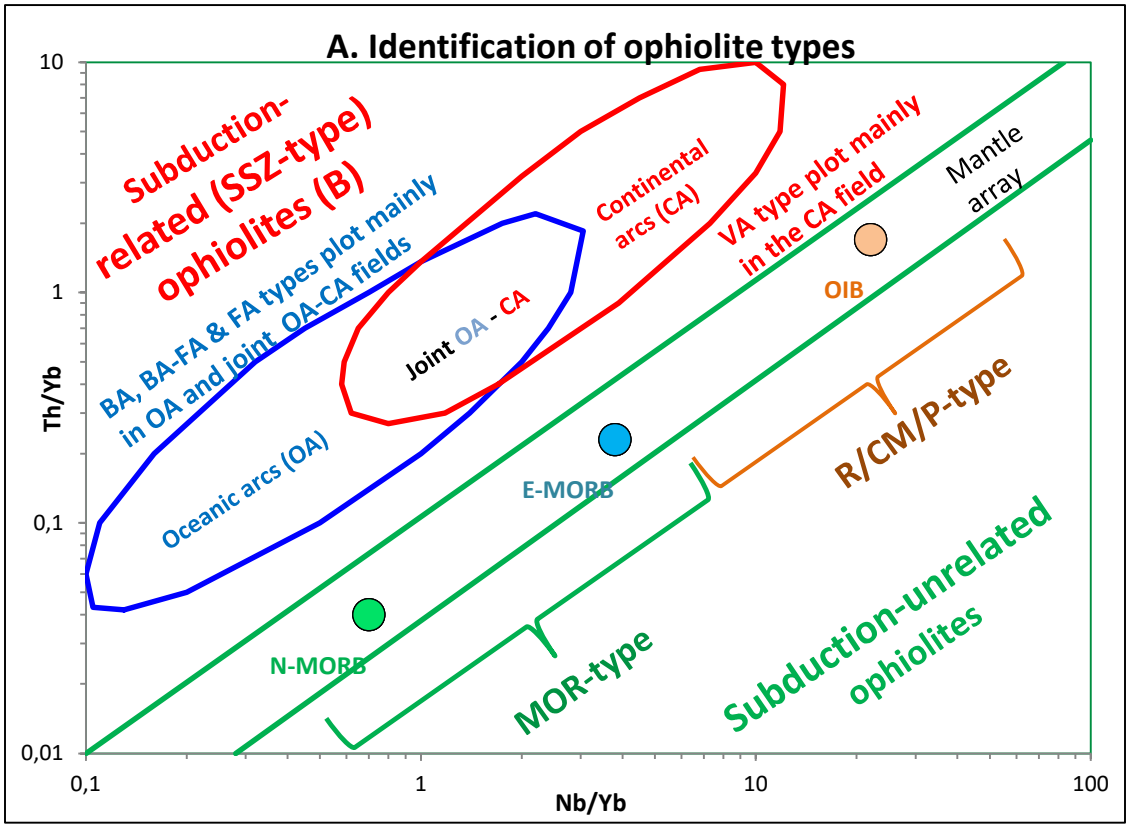


Figure 2

Click here to access/download;figure;Fig. 02. Discrimination diagrams.pdf



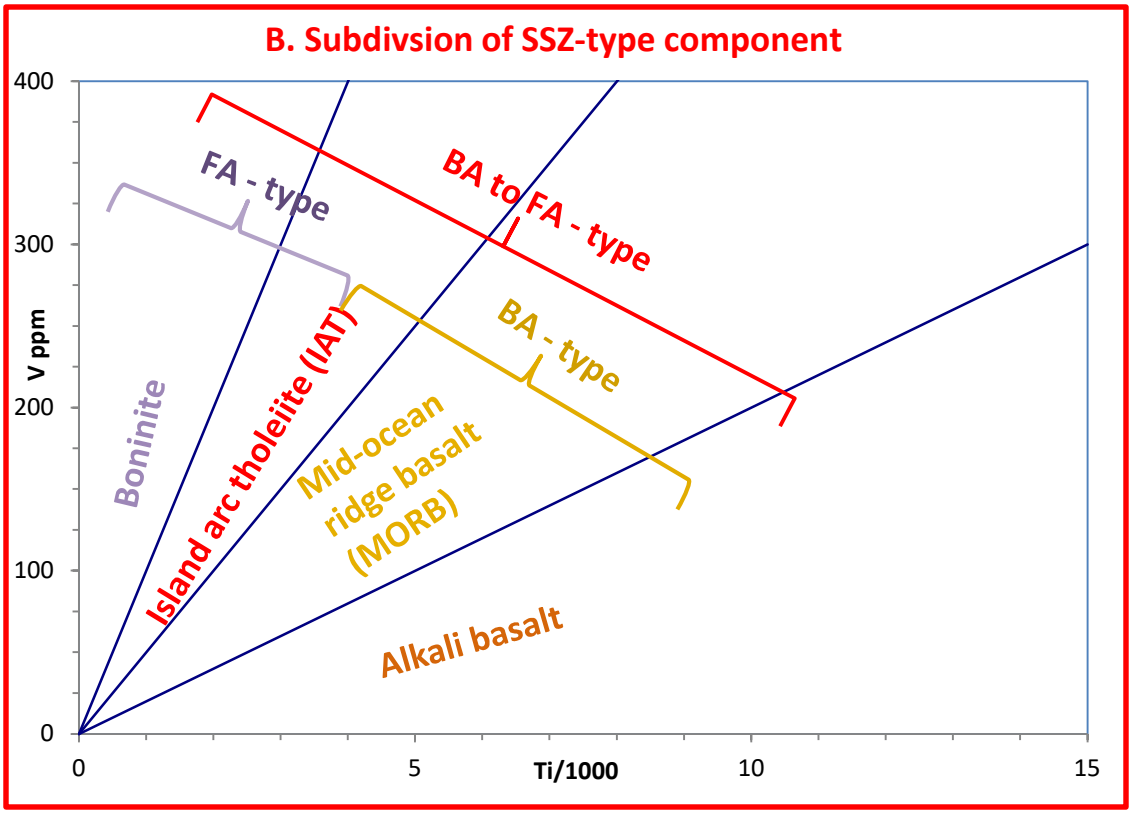


Figure 3

Click here to access/download;figure;Fig. 03. Cu histograms for all ophiolites.pdf

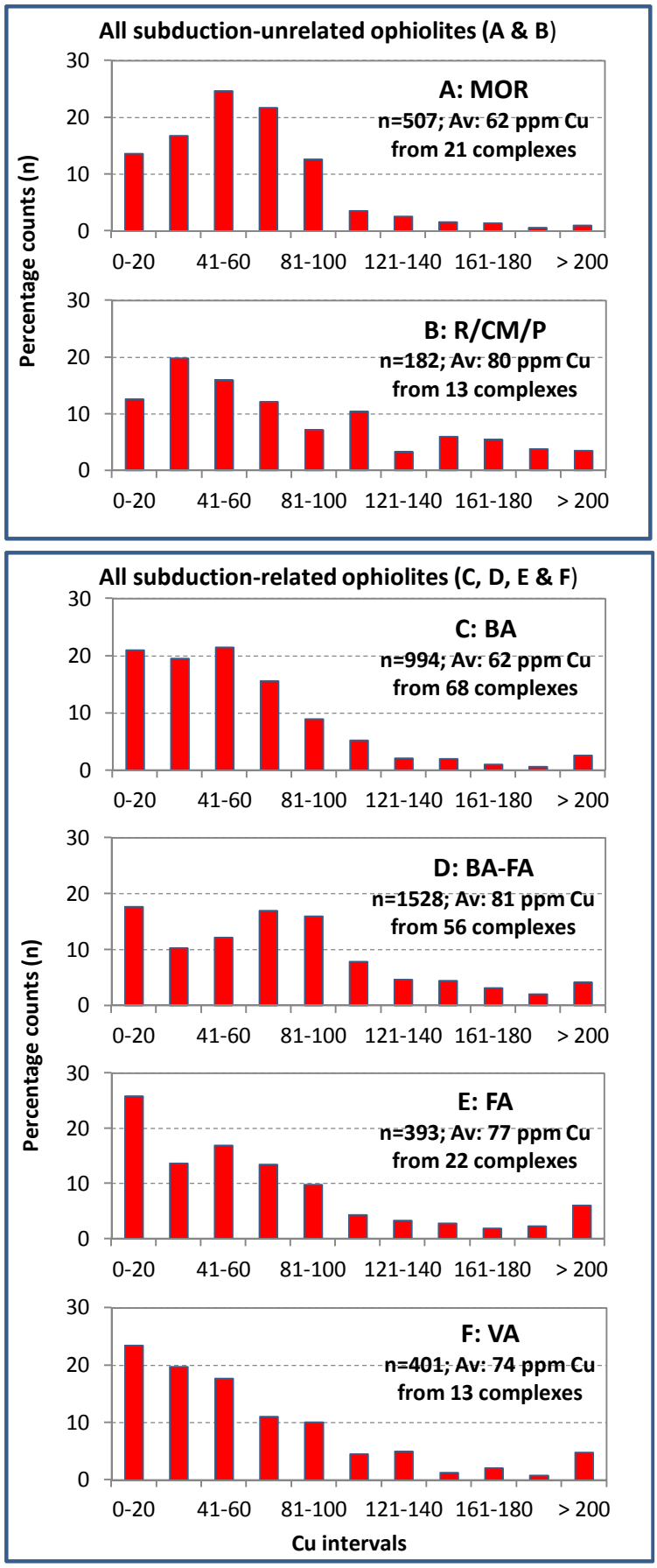


Figure 4

Click here to access/download;figure;Fig. 04. Zn histograms for all ophiolites.pdf

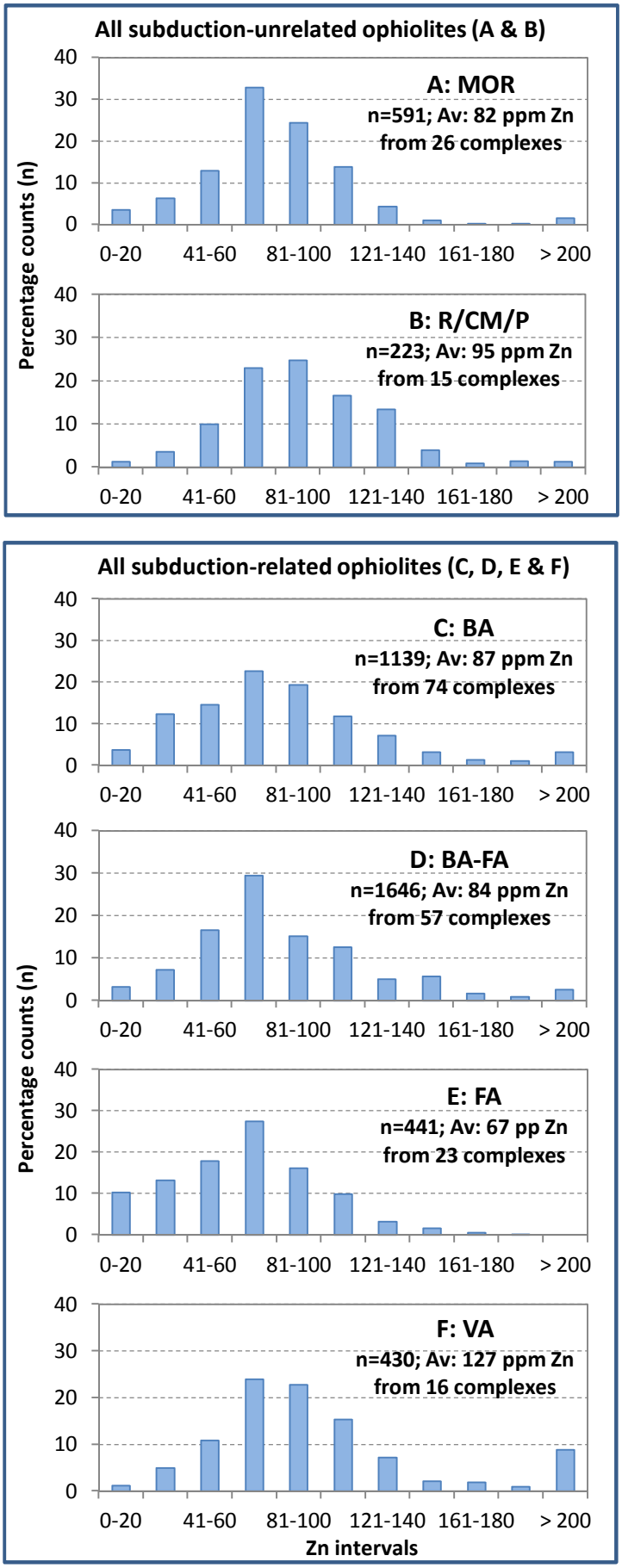


Figure 5

Click here to access/download;figure;Fig. 05. Pb histograms for all ophiolites.pdf

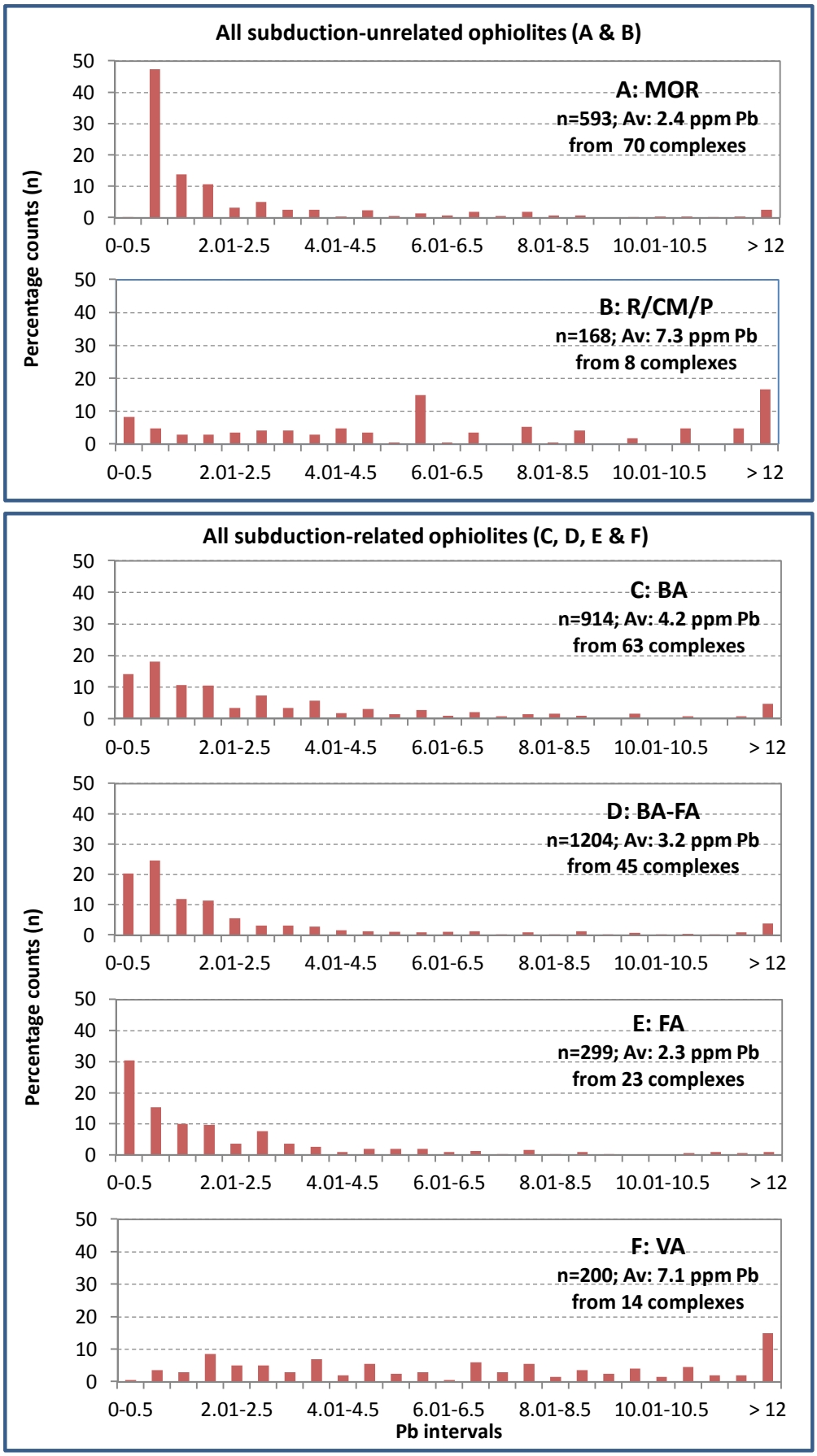


Figure 6

Click here to access/download;figure;Fig. 06. Ga histograms for all ophiolites.pdf

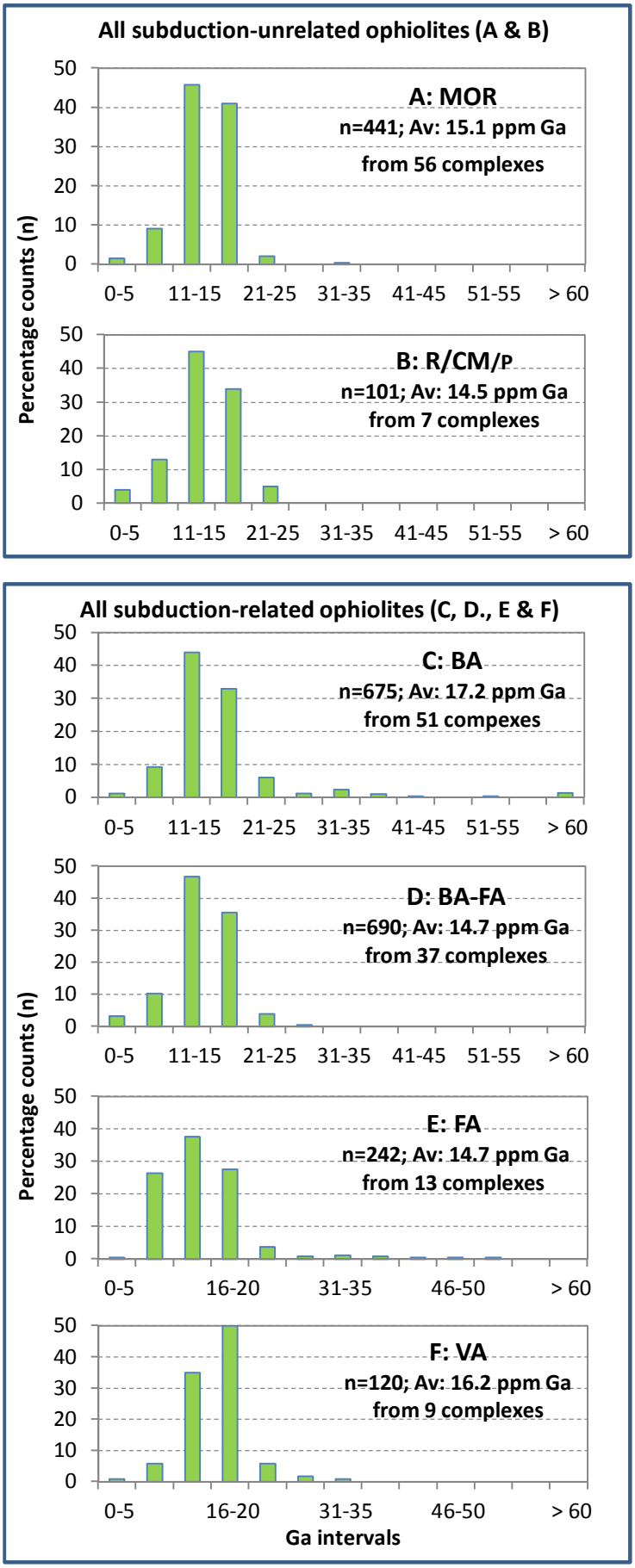


Figure 7

Click here to access/download;figure;Fig. 07. Cu, Zn, Pb & Ga histograms.pdf

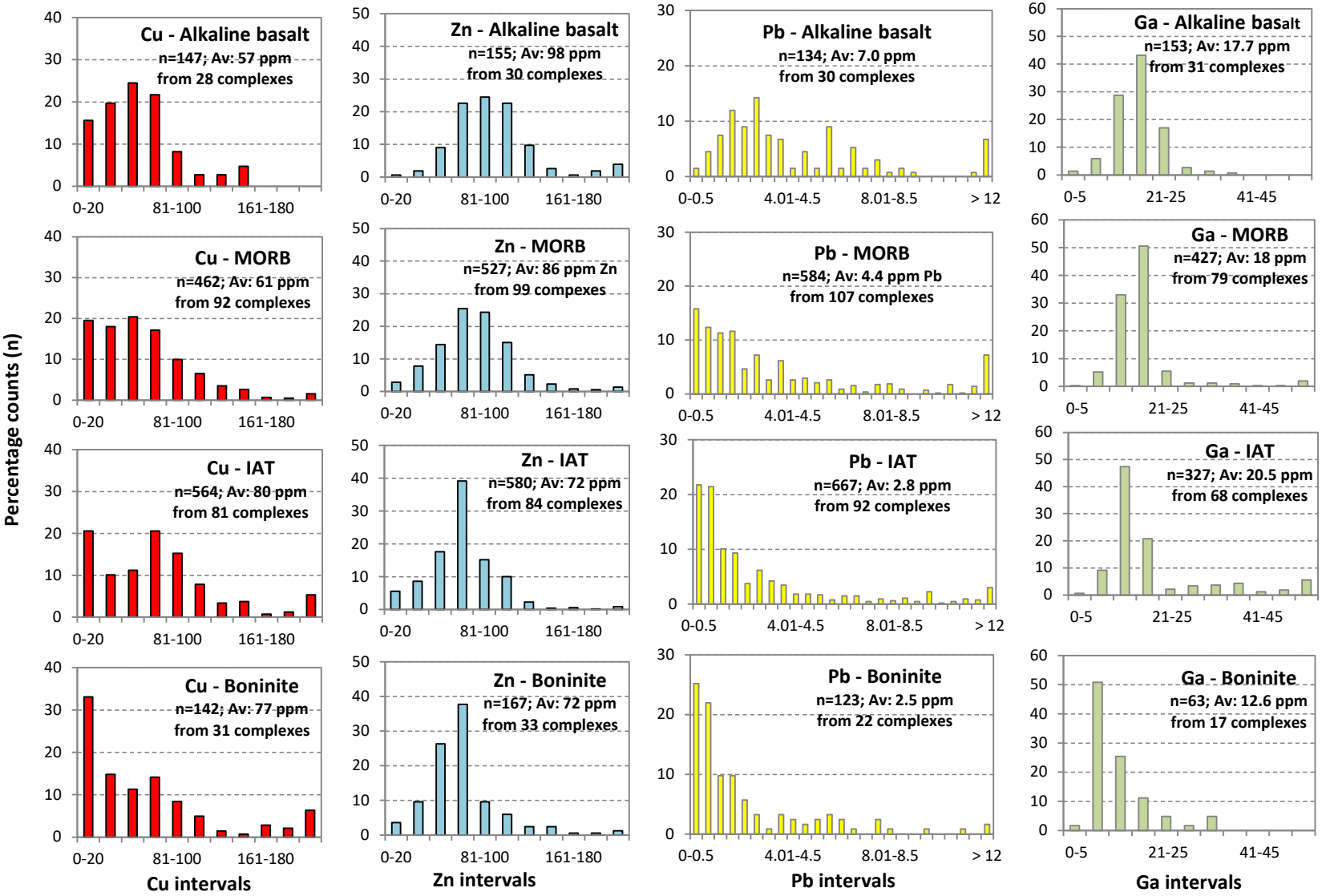


Figure 8

Click here to access/download;figure;Fig. 08. Histograms for mantle Cu, Zn, Pb & Ga.pdf

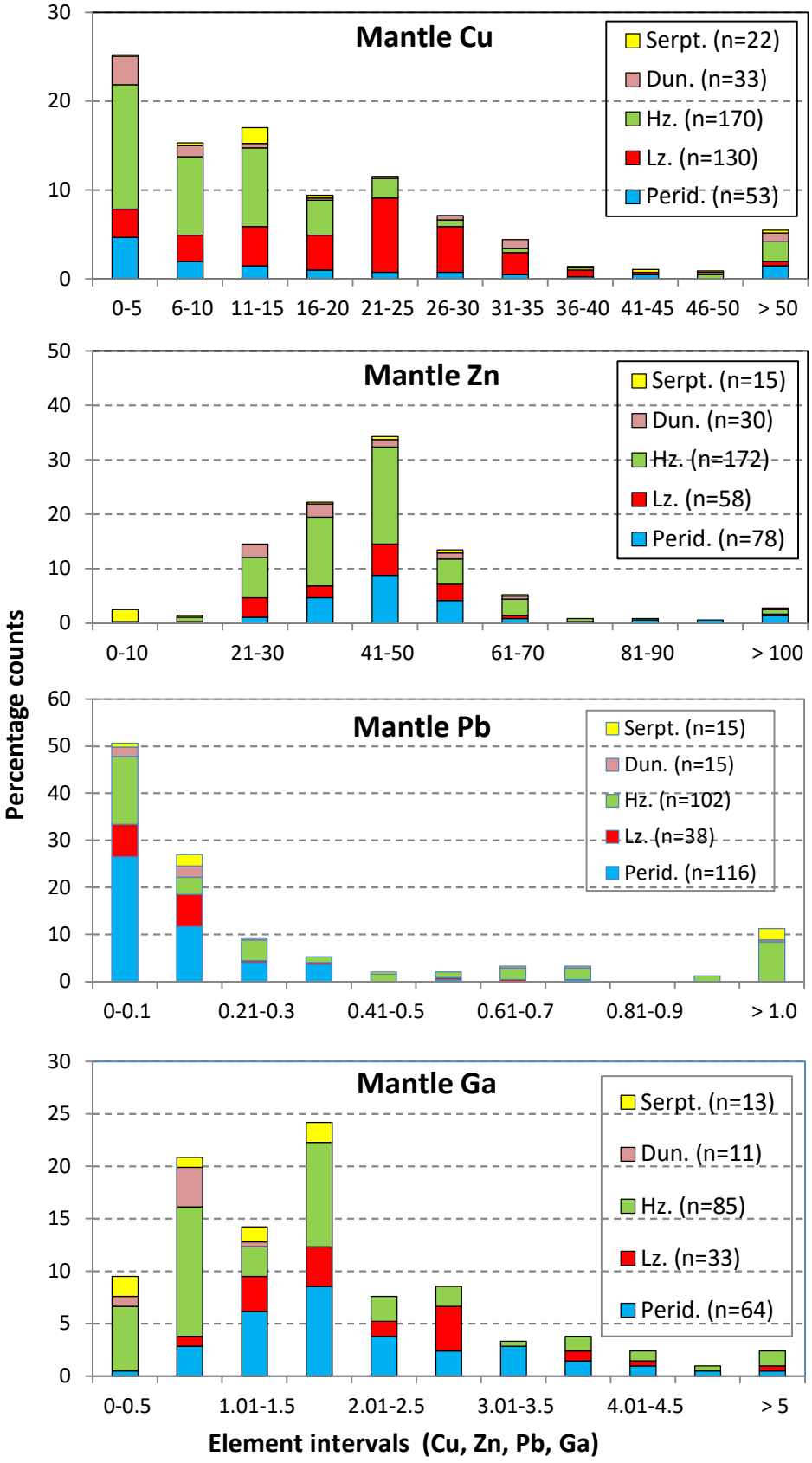
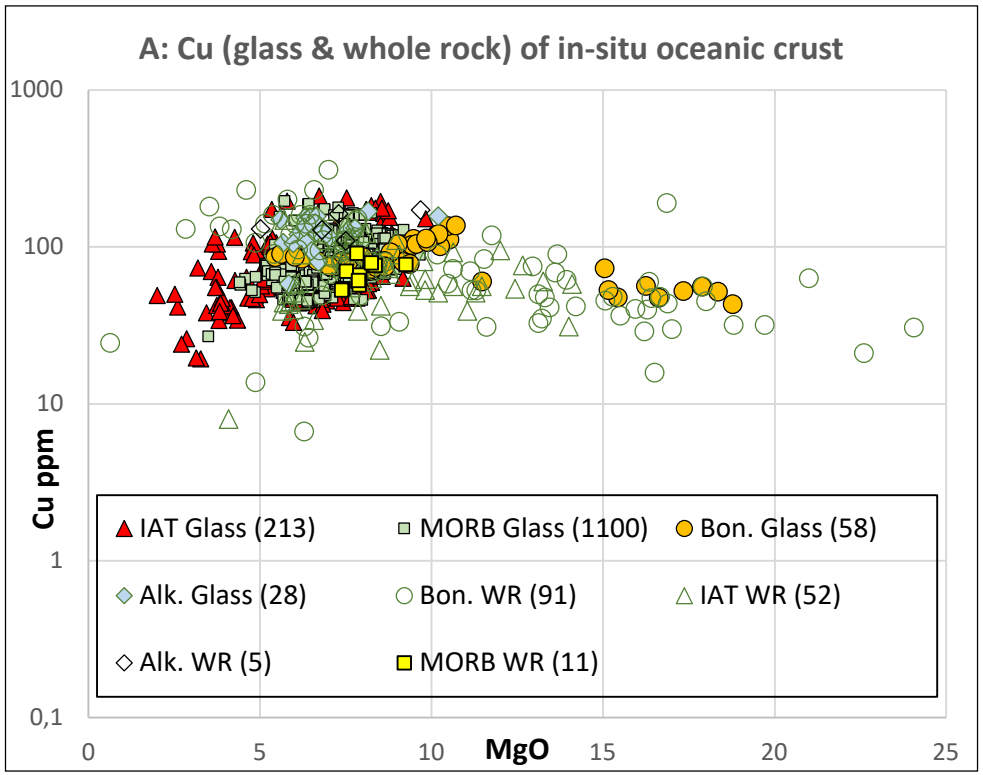


Figure 9

Click here to access/download;figure;Fig. 09. Cu distribution of in-situ oceanic crust and oph.pdf



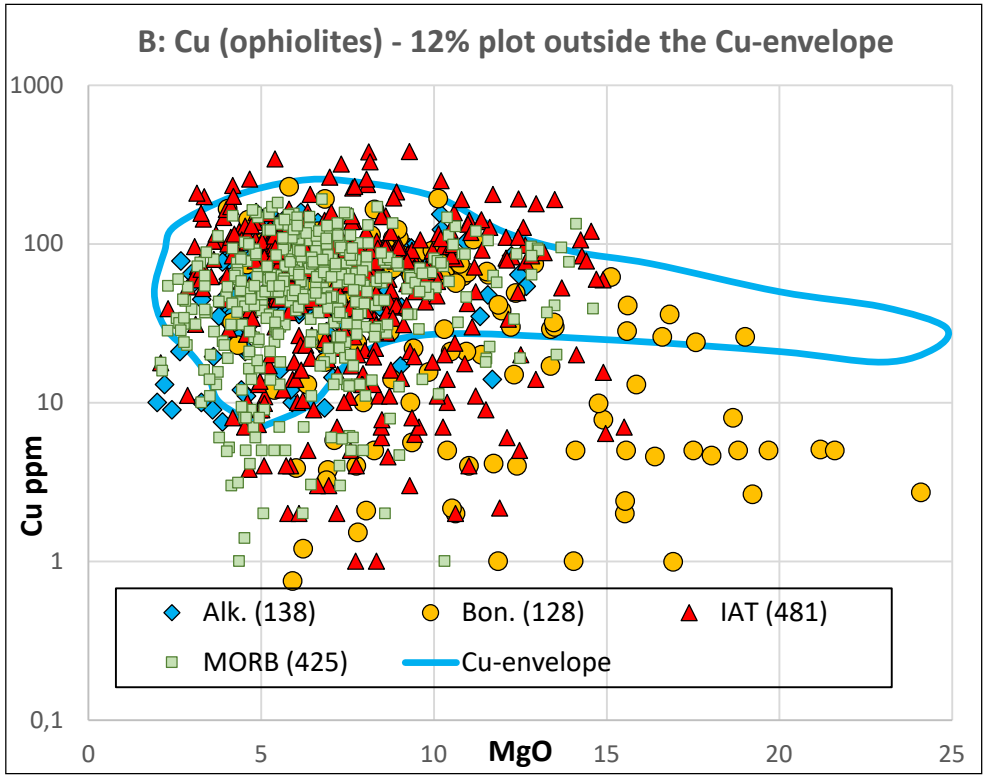


Figure 10

Click here to access/download;figure;Fig. 10. Zn distrivution of in-situ oceanic crust and oph..pdf

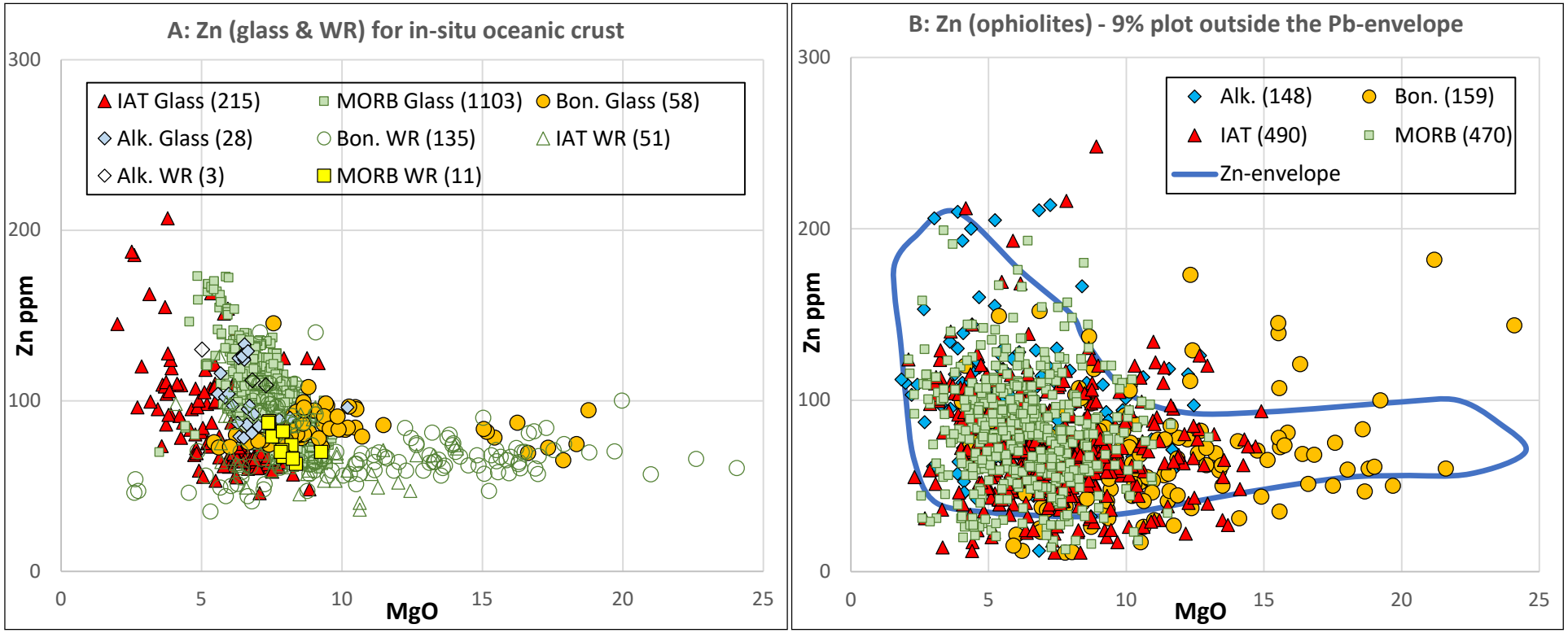


Figure 11

Click here to access/download;figure;Fig. 11. Pb distribution of in-situ oceanic crust and oph..pdf

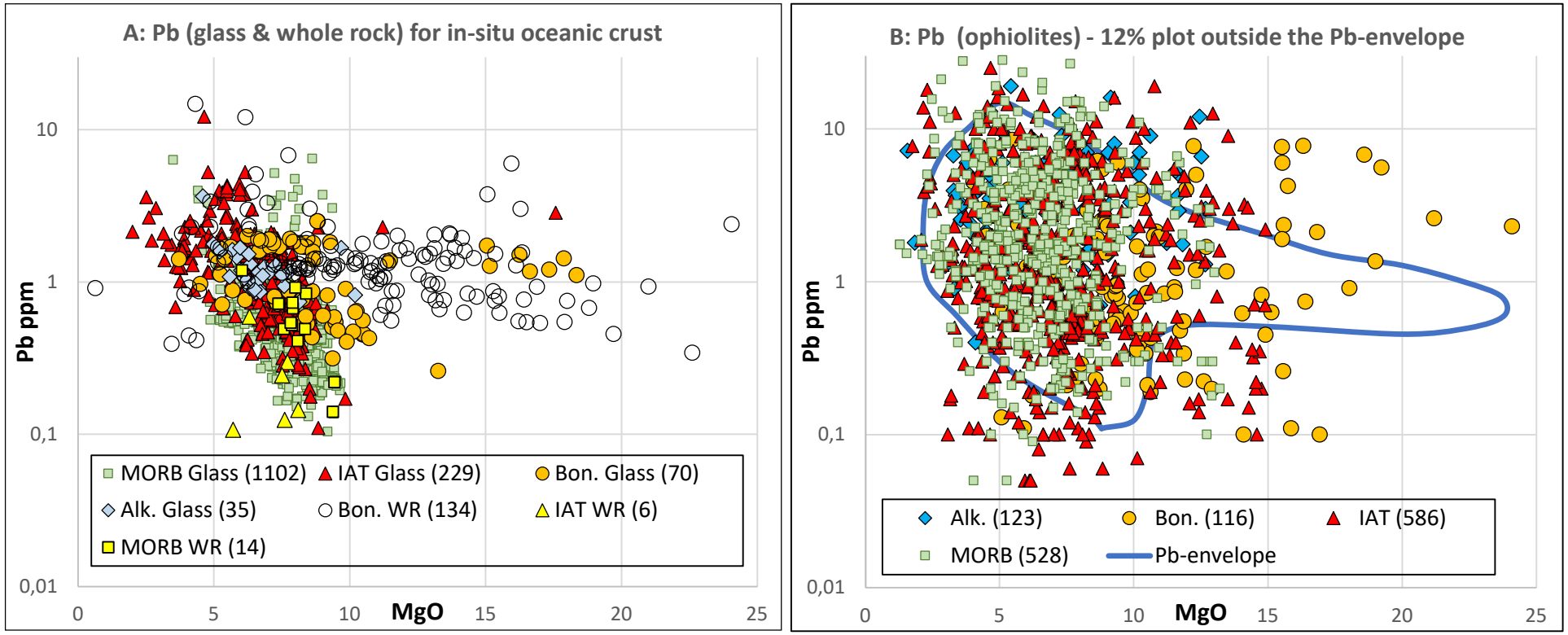


Figure 12

Click here to access/download;figure;Fig. 12. Ga distribution of in-situ oceanic crust and oph..pdf

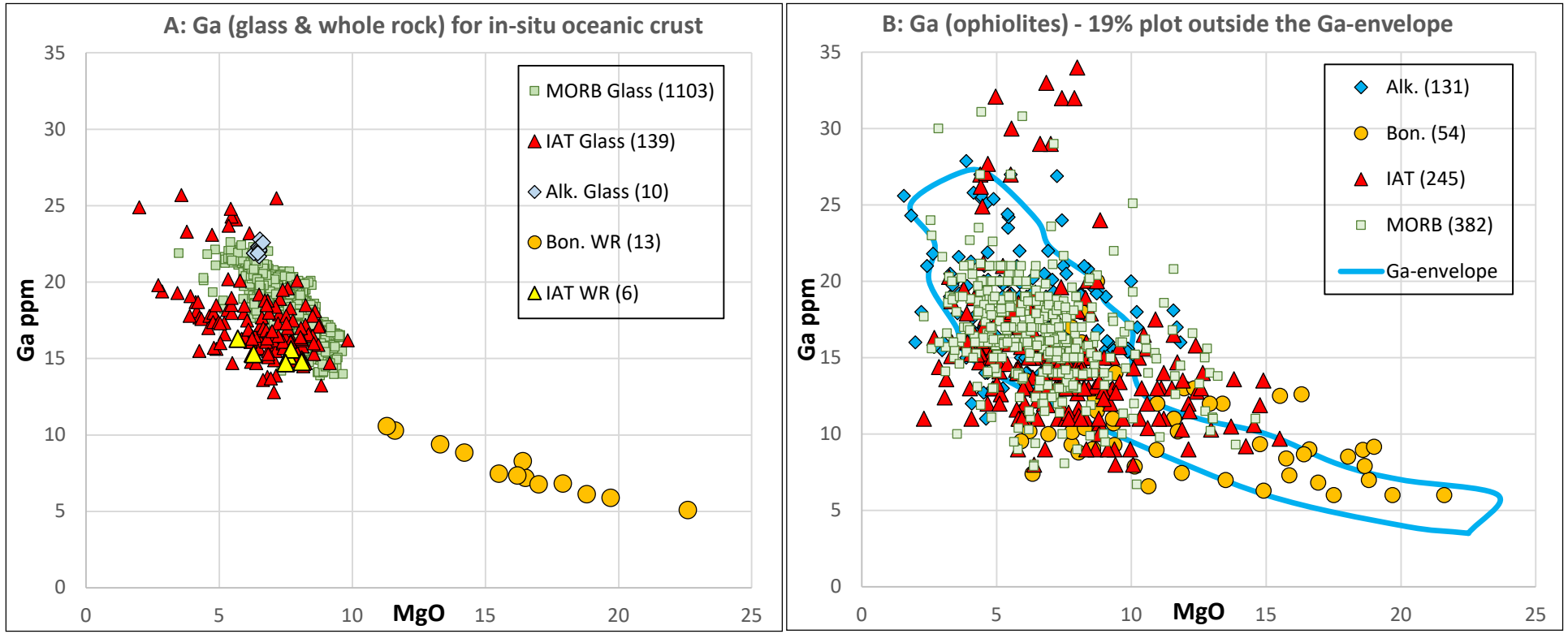
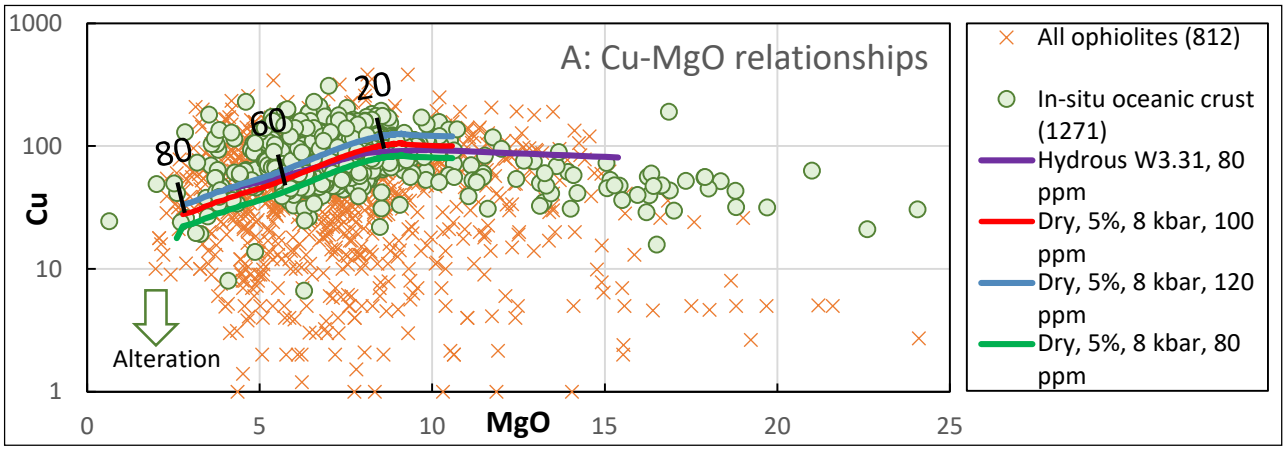
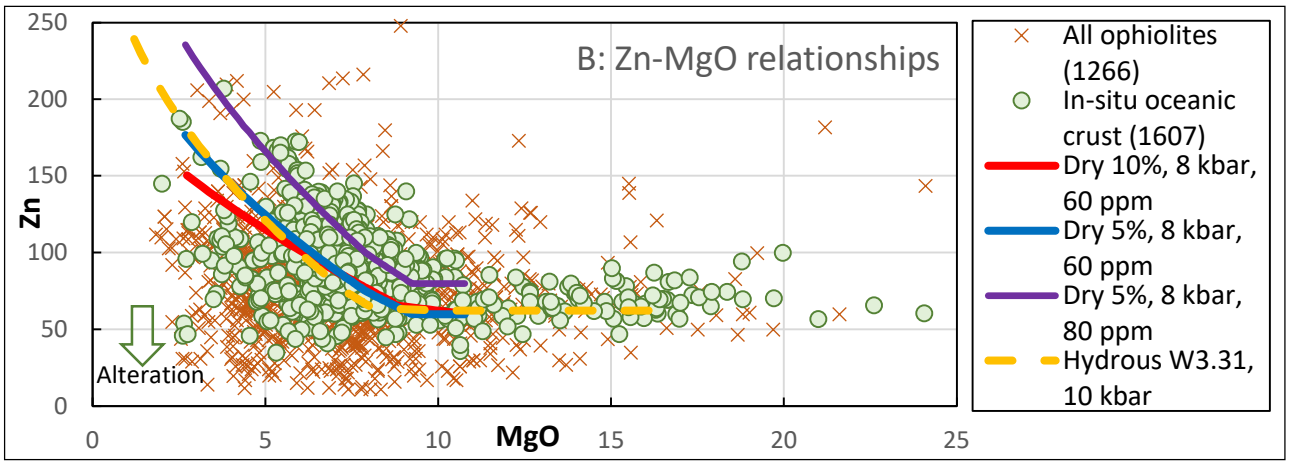
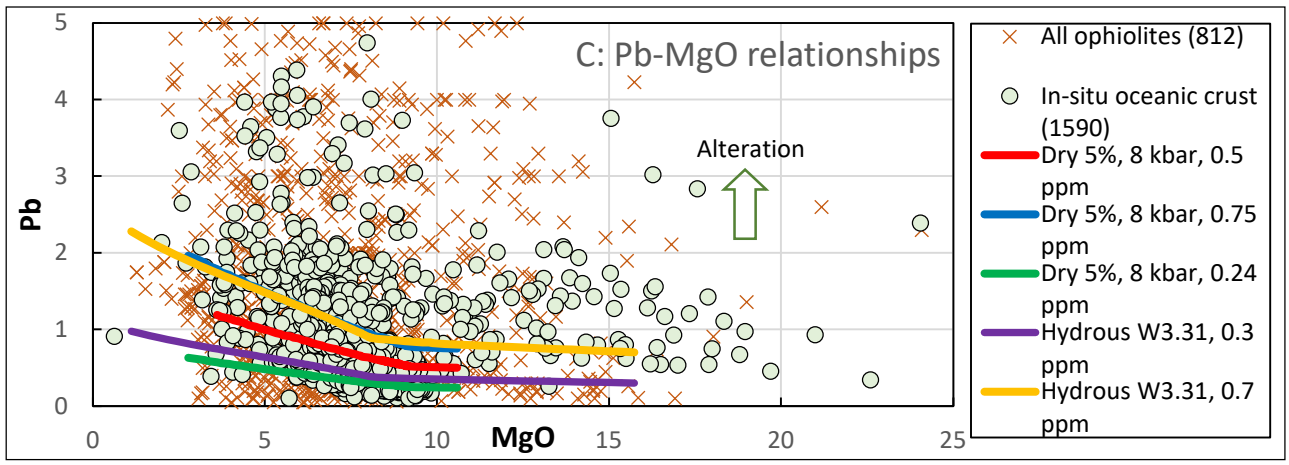


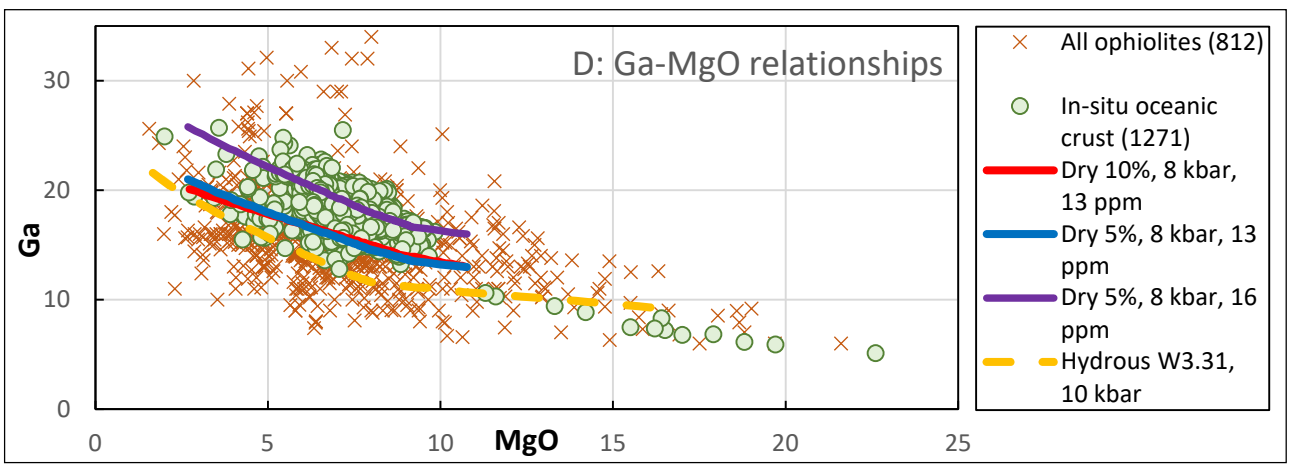
Figure 13

Click here to access/download;figure;Fig. 13. All elements +model lines.pdf









Supplementary Table #1



References for Supplementary Table #1

Click here to access/download
supplementary material
Refs to Supplementary Table 1.docx

Supplementary Table #2

Click here to access/download

supplementary material

Supplementary Table 2. Data from mantle rocks.xlsx

References for Supplementary Table #2

Click here to access/download
supplementary material
Refs to Supplementary Table 2.docx

Supplementary Table #3



References for Supplementary Table #3

Click here to access/download
supplementary material
References to Supplementary Table 3.docx